Evaluating the impact of post-processing medium-range ensemble streamflow forecasts from the European Flood Awareness System

Gwyneth Matthews[1], Christopher Barnard[2], Hannah Cloke[1,2,3,4,5], Sarah L Dance[1,6], Toni Jurlina[2], Cinzia Mazzetti[2], and Christel Prudhomme[2,7,8]

[1]Department of Meteorology, University of Reading, Reading, United Kingdom
[2]European Centre for Medium-range Weather Forecasts, Reading, United Kingdom
[3]Department of Geography and Environmental Science, University of Reading, Reading, United Kingdom
[4]Department of Earth Sciences, Uppsala University, Uppsala, Sweden
[5]Centre of Natural Hazards and Disaster Science, CNDS, Uppsala, Sweden
[6]Department of Mathematics and Statistics, University of Reading, Reading, United Kingdom
[7]Department of Geography, University of Loughborough, Loughborough, United Kingdom
[8]UK Centre for Ecology and Hydrology, Wallingford, United Kingdom

Correspondence: Gwyneth Matthews (g.r.matthews@pgr.reading.ac.uk)

Abstract. Streamflow forecasts provide vital information to aid emergency response preparedness and disaster risk reduction. Medium-range forecasts are created by forcing a hydrological model with output from numerical weather prediction systems. Uncertainties are unavoidably introduced throughout the system and can reduce the skill of the streamflow forecasts. Post-processing is a method used to quantify and reduce the overall uncertainties in order to improve the usefulness of the forecasts.

5 The post-processing method that is used within the operational European Flood Awareness System is based on the Model Conditional Processor and the Ensemble Model Output Statistics method. Using 2-years of reforecasts with daily timesteps this method is evaluated for 522 stations across Europe. Post-processing was found to increase the skill of the forecasts at the majority of stations both in terms of the accuracy of the forecast median and the reliability of the forecast probability distribution. This improvement is seen at all lead-times (up to 15 days) but is largest at short lead-times. The greatest improvement

10 was seen in low-lying, large catchments with long response times, whereas for catchments at high elevation and with very short response times the forecasts often failed to capture the magnitude of peak flows. Additionally, the quality and length of the observational time-series used in the offline calibration of the method were found to be important. This evaluation of the post-processing method, and specifically the new information provided on characteristics that affect the performance of the method, will aid end-users to make more informed decisions. It also highlights the potential issues that may be encountered

15 when developing new post-processing methods.

1 Introduction

Preparedness for floods is greatly improved through the use of streamflow forecasts resulting in less damage and fewer fatalities (Field et al., 2012; Pappenberger et al., 2015a). The European Flood Awareness System (EFAS), part of the European Commis-
sion's Copernicus Emergency Management Service, supports local authorities by providing continental-scale medium-range streamflow forecasts up to 15 days ahead (Thielen et al., 2009; Smith et al., 2016). These streamflow forecasts are produced by driving a hydrological model with an ensemble of meteorological forecasts from multiple numerical weather prediction (NWP) systems including two NWP ensembles and two deterministic NWP forecasts (Smith et al., 2016). However, the streamflow forecasts are subject to uncertainties that decrease their skill and limit their usefulness for end-users (Roundy et al., 2019;
Thiboult et al., 2017; Pappenberger and Beven, 2006). These uncertainties are introduced throughout the system and are often categorised as *meteorological uncertainties* (or input uncertainties) which propagate to the streamflow forecasts from the NWP systems, and *hydrological uncertainties* which account for all other sources of uncertainty including those from the initial hydrological conditions and errors in the hydrological model (Krzysztofowicz, 1999). It should be noted that throughout the paper meteorological uncertainties refers to the uncertainty in the streamflow forecasts that is due to the meteorological forc-
ings and not the uncertainty in the meteorological forecasts themselves. These differ as the meteorological variables are usually aggregated by the catchment system (Pappenberger et al., 2011). According to Krzysztofowicz (1999) and Todini (2008), a reliable forecast will include the total predictive uncertainty which is the probability of a future event occurring conditioned on all the information available when the forecast is produced.

Several approaches have been developed to reduce hydrological forecast errors and account for the predictive uncertainty.
Improvements to the NWP systems used to force the hydrological model have been shown to reduce the uncertainty in the streamflow forecasts (Dance et al., 2019; Flack et al., 2019; Haiden et al., 2021b). Additionally, the use of ensemble NWP systems to represent the uncertainty due to the chaotic nature of the atmosphere is becoming increasingly common and the use of multiple NWP systems can account for model parameter and structural errors in the meteorological forecasts (Wu et al., 2020; Cloke and Pappenberger, 2009). Regardless of whether deterministic or ensemble NWP systems are used, pre-processing
of the meteorological input can reduce biases and uncertainties often present in the forecasts (Verkade et al., 2013; Crochemore et al., 2016; Gneiting, 2014). Data assimilation schemes can be used to improve accuracy in the initial hydrological conditions (e.g. Liu et al., 2012; Mason et al., 2020) and calibration of the hydrological model can reduce model parameter uncertainties (Kan et al., 2019). To represent the hydrological uncertainties using an ensemble, similarly to the meteorological uncertainties, would require creating an ensemble of initial hydrological conditions and using several sets of model parameters or potentially
using multiple hydrological models (Georgakakos et al., 2004; Klein et al., 2020). Operationally this is usually prohibited by computational and temporal constraints particularly if an ensemble of meteorological forcings is already included. An alternative, relatively quick and computationally inexpensive approach is to post-process the streamflow forecasts.

Post-processing the streamflow forecast allows all uncertainties to be accounted for. Over the past few decades several tech-
niques have been proposed. These techniques can be split into two approaches: (1) methods accounting for the meteorological and hydrological uncertainties separately and (2) lumped approaches which calculate the total combined uncertainty of the

forecast. One of the first examples of the former approach was the Bayesian forecasting system which was applied to deterministic forecasts and consists of the Hydrological Uncertainty Processor (HUP Krzysztofowicz, 1999; Krzysztofowicz and Kelly, 2000; Krzysztofowicz and Herr, 2001; Krzysztofowicz and Maranzano, 2004) and an Input Uncertainty Processor (IUP Krzysztofowicz, 1999). The development of the Bayesian Ensemble Uncertainty Processor (Reggiani et al., 2009), an extension of the HUP for application in ensemble prediction systems, attempts to remove the need for the IUP by assuming the meteorological ensemble fully represents the input uncertainty. However, as streamflow forecasts are often under-spread this assumption is not always appropriate. The Model Conditional Processor (MCP) first presented in Todini (2008) also uses a conditional distribution-based approach by defining the joint distribution between the model output and the observations using a multi-variate Gaussian distribution. The MCP has the capacity to determine the total combined uncertainty if the joint distribution is defined between the observations and the forecasts of the operational system. To define this joint distribution a large set of historic forecasts is required which is not always available as operational systems are upgraded regularly. Therefore, often it is used to account for the hydrological uncertainty only (as it is in this paper, see Sect. 3). However, the method is attractive as it can be efficiently extended to allow for multivariate, multi-model, and ensemble forecasts (Coccia, 2011; Coccia and Todini, 2011; Todini, 2013; Todini et al., 2015). The method discussed in this study is partially motivated by the Multi-Temporal Model Conditional Processor (MT-MCP Coccia, 2011) which extends the original MCP method for application to multiple lead-times simultaneously.

Many regression-based methods have been developed to post-process streamflow forecasts because of their relatively simple structure (e.g. quantile regression (Weerts et al., 2011), indicator cokriging (Brown and Seo, 2010, 2013), and the General Linear Model Post-Processsor (Zhao et al., 2011)). The Ensemble Model Output Statistics (EMOS, Gneiting et al., 2005) method adjusts the mean and variance of an ensemble forecast using linear functions of the ensemble members and the ensemble spread respectively (Gneiting et al., 2005; Hemri et al., 2015a). This allows variations in ensemble spread to be used when estimating the predictive uncertainty. The strong autocorrelation in time observed in hydrological timeseries lends itself to the use of autoregressive error-models (e.g. Seo et al., 2006; Bogner and Kalas, 2008; Schaeybroeck and Vannitsem, 2011) although some of these methods do not account for uncertainty and instead try to correct errors in the trajectory of the forecast. These methods should therefore be used alongside a separate method which attempts to quantify the uncertainty. On the other hand, kernel-based (or "dressing") methods define a kernel to represent the uncertainty which is superimposed over the forecast or over every member for an ensemble forecast (Pagano et al., 2013; Verkade et al., 2017; Boucher et al., 2015; Shrestha et al., 2011). Depending on the approach used to define the kernel, this technique can account for the hydrological uncertainties or the total uncertainty but often requires a bias-correction method to be applied to the forecast beforehand (Pagano et al., 2013).

All the methods mentioned above, and many more that have not been mentioned (see Li et al., 2017, for a more comprehensive review), have been shown to be effective at improving the skill of forecasts in one or a few catchments. The Hydrological Ensemble Prediction Experiment (HEPEX, Schaake et al., 2007) post-processing intercomparison experiment resulted in comparisons between the different techniques (van Andel et al., 2013; Brown et al., 2013) but still relatively few studies have evaluated the performance of post-processing methods across many different catchments. Some exceptions include studies comparing the performance of post-processing techniques for limited numbers of basins in the USA (Brown and Seo (2013),

9 basins; Ye et al. (2014), 12 basins; and Alizadeh et al. (2020), 139 basins), and recently, Siqueira et al. (2021) evaluated two post-processing methods at 488 stations across South America. Skøien et al. (2021) compared variations of the EMOS method at the 678 stations across Europe and investigated the forecast features that indicated when post-processing was beneficial. However, as post-processing is incorporated into more large-scale, multi-catchment flood forecasting systems, such as the EFAS, there is a greater need to understand which ~~characteristics~~ catchment characteristics, as well as which forecast features, can affect the post-processing. In this paper, the operational post-processing method of the EFAS is evaluated at 522 stations to investigate how the performance of the post-processing method varies across the domain.

The EFAS domain covers hundreds of catchments across several hydroclimatic regions with different catchment characteristics. The raw forecasts (i.e. forecasts that have not undergone post-processing) have varying levels of skill across these catchments (Alfieri et al., 2014), and are regularly evaluated in order to identify possible areas of improvement and to allow end-users to understand the quality of the forecasts. At the locations of river gauge stations, where near real-time and historic river discharge observations are available, the raw forecasts are post-processed using a post-processing method which is motivated by the MCP and EMOS techniques. However, the post-processed forecasts do not currently undergo regular evaluation. This study aims to assess the post-processing method used within the EFAS. Additionally, new information is provided about the effect that characteristics of the catchments and properties of the forecasting system have on the performance of the post-processing method. Specifically, the paper will address the following questions:

– Does the post-processing method provide improved forecasts?

– What affects the performance of the post-processing method?

The remainder of the paper is set out as follows. In Sect. 2 we briefly describe the EFAS system used to produce forecasts operationally. In Sect. 3 we introduce the post-processing method being evaluated and explain in detail how the post-processed forecasts are created. In Sect. 4, the evaluation strategy is described. This includes an explanation of the criteria used to select stations, details of the reforecasts used in this evaluation, and a description of the evaluation metrics considered. We separate the results section (Sect. 5) into two main sub-sections. In Sect. 5.1 we assess the affect of post-processing on different features of the forecast such as the forecast median and the timing of the peak. In Sect. 5.2 we investigate how the benefits of post-processing vary due to different catchment characteristics such as response time and elevation. Finally, in Sect. 6 we state our conclusion that post-processing improves the skill of the streamflow forecasts for most catchments and highlight the main factors affecting the performance of the post-processing method.

2 European Flood Awareness System (EFAS)

The ~~EFAS produces a range of streamflow forecast products for catchments across Europe. The~~ focus of this paper is the evaluation of the post-processing method used operationally to create the product referred to as the 'real-time hydrograph' (see Fig. 4). In ~~the current~~ this section, we describe the ~~operational~~ production of the (raw) EFAS medium-range ensemble forecasts that are inputs for the post-processing method described in Sect. 3. ~~Operationally,~~ The EFAS system has recently been updated,

therefore reforecasts are used in this study allowing for a larger number of forecasts to be evaluated. Reforecasts are forecasts for past dates created using a forecasting system as close to the operational system as possible (Hamill et al., 2006; Harrigan et al., 2020)

120 . However, there are differences between the reforecasts and the medium-range ensemble forecasts are the foundation of several forecast products and are generated twice daily at 00 UTC and 12 UTC with a maximum lead-time of 15 days (Smith et al., 2016). Version 4 of EFAS (operational October 2020) produces forecasts with a 6-hourly timestep and at a resolution of 5 km x 5 km on a Lambert Azimuthal Equal Area Projection (Mazzetti et al., 2021b). It should be noted that post-processing is currently only performed at daily timesteps and requires the raw forecasts described here to be temporally

125 aggregated.

The EFAS medium-range forecasts are created by driving a hydrological model, LISFLOOD, with the output from multiple NWP systems. For the forecast, the required meteorological forcings are operational system due to limited computational resources and data latency in the operational system. Therefore, we also highlight the differences between the evaluated reforecasts and the precipitation, temperature, and potential evaporation fields from the NWP systems (Smith et al., 2016; EFAS, 2020)

130 . Operationally, four meteorological forecast products are used to drive LISFLOOD: two deterministic forecasts and two ensemble forecasts. The European Centre for Medium-range Weather Forecasts (ECMWF) provides (1) a deterministic forecast with a spatial resolution of 9 km and a maximum lead-time of 10 days, operational forecasts.

Version 4 of EFAS (operational October 2020) uses the LISFLOOD hydrological model at the increased temporal resolution of 6 hours and (2) a 51-member ensemble forecast with a spatial resolution of 18 km and a maximum lead-time of 15 days

135 (EFAS, 2020). Both ECMWF forecasts are created using the ECMWF Integrated Forecasting System (currently Cycle 47r2, Haiden et al., 2 . The German Weather Service (DWD) also provides (3) a high-resolution deterministic forecast. This forecast has a maximum lead-time of 7 days. The first 3 days are created using the COnsortium for Small-scale MOdelling - EUrope (COSMO-EU) model which has a spatial resolution 6.5 km (Baldauf and Wetterdienst, 2014; Deutscher Wetterdienst, 2015a). Days 4 to 7 are created using the DWD's ICON global model which has a spatial resolution 13 km (Zängl et al., 2015; Deutscher Wetterdienst, 2015b)

140 . The final forecast is (4) a 20-member ensemble forecast produced using the COnsortium for Small-scale Modelling's Limited-area Ensemble Prediction System (COSMO-LEPS, Montani et al., 2011; COSMO, 2020). The COSMO-LEPS forecast has a maximum lead-time of 5 days and a spatial resolution of 7 km but has a smaller domain than the other NWP systems (see Fig. 1 in Smith et al. (2016) and Fig.1 in Arnal et al. (2019)). The forecast fields are regridded to fit the EFAS domain and used as input for the LISFLOOD hydrological model (Smith et al., 2016).

145 The LISFLOOD hydrological model 5 km (Mazzetti et al., 2021b). LISFLOOD is a GIS-based spatially distributed gridded rainfall-runoff-routing model specifically designed to replicate the hydrological processes of large catchments (Van Der Knijff et al., 2010; De Roo et al., 2000). The parameters controlling the processes within At each timestep LISFLOOD calculates the discharge as the average over the previous 6 hours for each grid-box are determined in an offline in the EFAS domain. For EFAS 4 the model calibration of LISFLOOD which has recently been performed for the release of EFAS 4 (Mazzetti et al., 2021b)

150 . For each grid-box in the EFAS domain LISFLOOD calculates the average discharge at 6-hourly timesteps was performed using a mixture of daily and six hourly observations where available for the period 1990-2017 (Mazzetti et al., 2021a; Mazzetti and Harrigan, 202 . The reforecasts used in this evaluation are created using the same hydrological model.

Operationally, the medium-range ensemble forecasts are generated twice daily at 00 UTC and 12 UTC with a maximum lead-time of 15 days (Smith et al., 2016). The forecasts are created by forcing LISFLOOD with the precipitation, temperature, and potential evaporation outputs from four NWP systems (Smith et al., 2016; EFAS, 2020): two deterministic forecasts and two ensemble forecasts. For further information about the NWP systems see EFAS (2020). The reforecasts used in this study are generated twice weekly at 00 UTC on Mondays and Thursdays by forcing LISFLOOD with reforecasts from the European Centre of Medium-Range Weather Forecasts (ECMWF) ensemble system which have 11 ensemble members.

The hydrological initial conditions for the streamflow forecasts are determined by forcing LISFLOOD with meteorological observations to create a simulation henceforth referred to as the *water balance simulation*. The water balance simulation provides would provide the starting point of the forecast in terms of water storage within the catchment and discharge in the river. The precipitation and temperature point-observations (collected by the Meteorological Data Collection Centre of the Copernicus Emergency Management Service) are interpolated using the SPHEREMAP algorithm to the 5 x 5 km EFAS domain (Smith et al., 2016; Arnal et al., 2019). The water balance simulation may contain errors due meteorological observation errors and structural errors in the hydrological model. Therefore, the water balance simulation may not represent the true state of the physical system, introducing uncertainty to the streamflow forecast. Operationally, there is a However, there is an operational time delay in receiving the meteorological observations of 18 hours for the 00 UTC cycle and 30h for the 12 UTC cycle. The . Therefore, the deterministic meteorological forecasts are used to drive the LISFLOOD model for the time period between the last available meteorological observation and the initial timestep of the forecast in a process called the 'fill-up'. For the reforecasts, all necessary meteorological observations are available so there is no need for the fill-up process.

3 Post-processing method

This section describes the post-processing method evaluated. Post-processing is performed at stations for which near real-time and historic river discharge observations are available. The method is motivated by the Multi-Temporal Model Conditional Processor (MT-MCP, Coccia, 2011) and Ensemble Model Output Statistics (EMOS, Gneiting et al., 2005) which are used to quantify the hydrological and meteorological uncertainties, respectively. The Kalman filter is then used to combine these uncertainties. Since these methods assume Gaussianity, the Normal Quantile Transform (NQT) is used to transform the discharge values from physical space to standard Normal space. As with many post-processing methods, an offline calibration is required to define a so-called *station model*. In Sect. 3.1 some notation is introduced. Details on the post-processing method are given in Sects. 3.2 to 3.4. Figure 1 outlines the structure of the method. A discussion of the input data is postponed until Sect. 4.2.

3.1 Notation

In this section notation and definitions used throughout the paper are introduced. The aim of post-processing is to correct the errors and account for the uncertainty that may be present in a forecast. As described in Sect. 2, the EFAS produces ensemble streamflow forecasts for the whole of Europe on a 5 km x 5 km km grid with 6-hourly timesteps. However, post-processing is performed at daily timesteps and only at stations for which near real-time and historic river discharge observations are available.
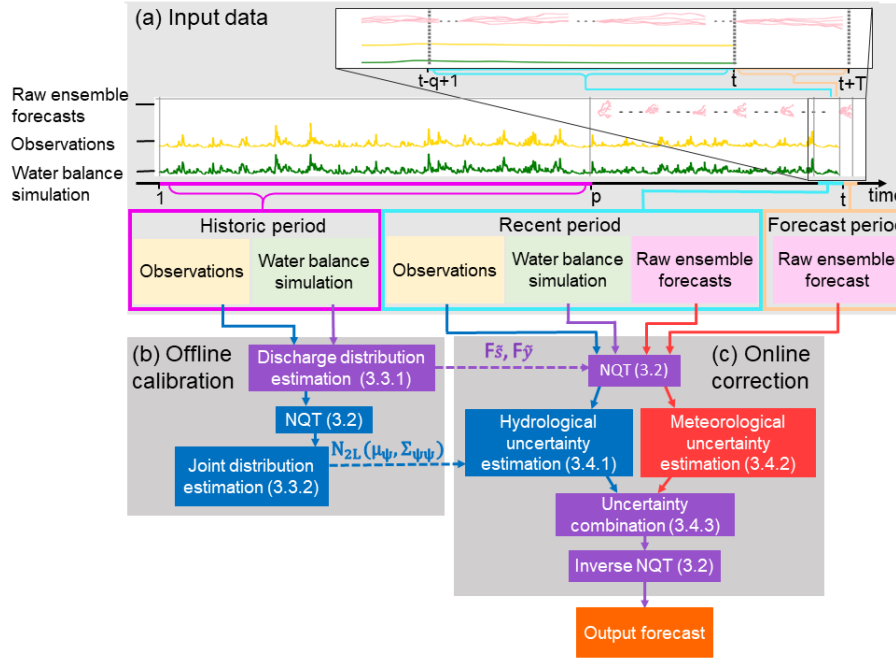
Figure 1. Flow chart describing the post-processing method at a station. (a) Input data are separated by time period (historic period: fuchsia, recent period: cyan, forecast period: peach) and by data type (observations: yellow, water balance simulations: green, raw ensemble forecasts: pink). The top time-series is a magnification of the bottom time-series for the period $t-q+1$ to $t+T$. The historic period has length p. For a forecast produced at time t, the recent period starts at time $t-q+1$ and the forecast period ends at time $t+T$. (b) Offline calibration steps. (c) Online correction steps. NQT is the Normal Quantile Transform. Blue and red arrows and boxes show the data and methods used to account for the hydrological uncertainty and the meteorological uncertainty, respectively. Data and methods used to account for both the hydrological and meteorological uncertainties are shown in purple. Dashed arrows show data stored in the station model such as the cumulative distribution functions of the water balance simulation and observations, denoted $F_{\tilde{s}}$, and $F_{\tilde{y}}$, respectively, and the joint distribution between the water balance simulation and observations, denoted $\cancel{N_{2L}(\boldsymbol{\mu}_{\phi}, \boldsymbol{\Sigma}_{\phi\phi})} \underbrace{N_{2L}(\boldsymbol{\mu}_{\psi}, \boldsymbol{\Sigma}_{\psi\psi})}$. Section numbers given in parentheses contain more details.

185   Therefore, the discharge values corresponding to the grid-boxes representing the locations of the stations are extracted and temporally aggregated to daily timesteps. This creates a separate streamflow forecast for each station and it is these single station forecasts that are henceforth referred to as the *raw forecasts*. The post-processing method evaluated in this paper is applied separately at each station creating a corresponding *post-processed forecast* for each raw forecast.

     The input data shown in Fig. 1a is the input data required for the post-processing of a single raw forecast (i.e. for one station).

190   As shown, the input data can be separated into three time periods. These time periods are henceforth referred to (from left to right in Fig. 1a) as the *historic period*, the *recent period*, and the *forecast period*. The length of the historic period, denoted p, varies between stations depending on the length of the historic observational record available. However, a minimum of 2 years of observations since 1991 is required for the offline calibration. For a forecast produced at time t, the recent period has

q timesteps and extends from time $t - q + 1$ to time t. The forecast period extends from time $t + 1$ to time $t + T$ for a forecast with a maximum lead-time of T timesteps. The length of the recent period and the forecast period combined is $L = q + T$. For convenience, we introduce a *timestep notation* of the form $t_i : t_j$ to represent all timesteps between time t_i and time t_j i.e. $t_i : t_j$ means $t_i, t_i + 1, t_i + 2, \ldots t_j - 1, t_j$.

The raw ensemble forecast that is post-processed is the only data available in the forecast period. This forecast is produced at time t, has M ensemble members, and a maximum lead-time of T timesteps. The full ensemble forecast is represented by a matrix, denoted $\tilde{\mathbf{x}}_t(t + 1 : t + T) \in \mathbb{R}^{T \times M}$, where each column corresponds to an ensemble member and contains a vector of discharge values for each timestep in the forecast period. ~~Here~~Throughout the paper, the tilde notation indicates that the discharge values are in physical space ~~, the~~ whereas discharge values without the tilde are in the standard Normal space (see Sect. 3.2). The subscript t indicates the forecast production time, and the range of timesteps for which discharge values are available is shown using the timestep notation. The raw ensemble forecasts from the recent period are denoted using similar notation such that, for example, the forecast produced at $t - q + 1$ is denoted $\tilde{\mathbf{x}}_{t-q+1}(t - q + 2 : t - q + 1 + T) \in \mathbb{R}^{T \times M}$. All forecasts are from the same forecasting system and so all have M ensemble members and maximum lead-times of T timesteps.

The time-series of observations for a single station is denoted by the vector $\tilde{\mathbf{y}}$ where each element represents a daily discharge observation. The observations in the historic period are used in the offline calibration (see Fig. 1b and Sect. 3.3) and are denoted $\tilde{\mathbf{y}}(1 : p) \in \mathbb{R}^p$ where the timestep notation is used to show the range of timesteps for which observations are available. This vector is the same for all forecasts for this station as the station model is not updated between forecasts. The observations in the recent period (the q timesteps up to the production time of the forecast) are used in the online correction (see Fig. 1c and Sect. 3.4) and are denoted $\tilde{\mathbf{y}}(t - q + 1 : t) \in \mathbb{R}^q$. Since $\tilde{\mathbf{y}}(t - q + 1 : t)$ is a function of t the observations in this vector are different for each forecast production time.

Similarly, the time-series of the water balance simulation, denoted by the vector $\tilde{\mathbf{s}}$, is used in both the offline calibration and the online correction. Each element of the vector represents a daily water balance simulation value calculated by forcing LISFLOOD with meteorological observations (see Sect. 2). The water balance simulation values from the historic period, $\tilde{\mathbf{s}}(1 : p)$, are selected to correspond to the timesteps of the p observations from the same period. The water balance simulation values from the recent period are denoted $\tilde{\mathbf{s}}(t - q + 1 : t)$ and are dependent on the forecast production time, t.

3.2 Normal Quantile Transform (NQT)

The methods used in this post-processing method utilise the properties of the Gaussian distribution but discharge values usually have highly skewed non-Gaussian distributions (Hemri, 2018). Therefore, the NQT is used to transform the discharge data to the standard Normal distribution which has a mean of zero and a variance of 1, denoted $N(0, 1)$. The NQT is applied separately to all input data (observed, simulated, and forecast) for a given station, therefore, it is defined here for any scalar discharge value $\tilde{\eta}$. ~~The transformed discharge values are distinguished from the discharge values in physical space by the removal of the tilde notation (e.g. η).~~

The NQT defines a one-to-one map between the quantiles of the Cumulative Distribution Function (CDF) of the discharge distribution in physical space, $F_{\tilde{\eta}}(\tilde{\eta})$, and the CDF of the standard Normal distribution, $Q(\eta)$. The scalar function $F_{\tilde{\eta}}$ is

dependent on whether $\tilde{\eta}$ represents a modelled discharge value (simulated or forecast) or an observed discharge value. The calculation of the discharge distributions and their subsequent CDFs are described in Sect. 3.3.1. The NQT transforms each scalar discharge value such that

$$\eta = Q^{-1}\left(F_{\tilde{\eta}}\left(\tilde{\eta}\right)\right). \tag{1}$$

After the forecast values have been adjusted by the post-processing method, the inverse NQT,

$$\tilde{\eta} = F_{\tilde{\eta}}^{-1}\left(Q\left(\eta\right)\right), \tag{2}$$

is applied to transform the discharge values from the standard Normal space back to the physical space (see Fig. 1c).

3.3 Offline calibration

The offline calibration (see Fig. 1b) has two main aims: to determine the distributions of the observed, $\tilde{\mathbf{y}}$, and simulated, $\tilde{\mathbf{s}}$, discharge values at a station, and to define the joint distribution between the transformed observations, $\mathbf{y}$, and the transformed water balance simulation, $\mathbf{s}$. These distributions are then stored in the station model for use in the online post-processing step (shown by dashed lines in Fig. 1). The input data required for the offline calibration is an historic record of observations for the station, denoted by the vector $\tilde{\mathbf{y}}(1:p) \in \mathbb{R}^p$, and, for the same period, an historic time-series of the water balance simulation for the grid-box representing the location of the station, denoted by the vector $\tilde{\mathbf{s}}(1:p) \in \mathbb{R}^p$, where the tilde notation signifies the variables are initially in physical space. The length of these vectors, p, is equal to the number of data points in the historic records and varies between stations. A minimum of 2 years historic data is required to guarantee that $p >> L$ (see Sect. 3.1).

3.3.1 Discharge distribution approximation

The NQT requires the Cumulative Distribution Function (CDF) of the observed and simulated discharge values in physical space, denoted $F_{\tilde{y}}$ and $F_{\tilde{s}}$ respectively, to be defined. This section describes the approach used to estimate these functions.

First, the discharge density distributions are estimated using the observations, $\tilde{\mathbf{y}}(1:p) \in \mathbb{R}^p$, and the water balance simulation values, $\tilde{\mathbf{s}}(1:p) \in \mathbb{R}^p$, from the historic period. These historic time-series are often only a few years long and therefore may not represent the full discharge distribution due to the relative rarity of larger discharge values. To avoid the issues that short time-series commonly cause in the inverse NQT (discussed in Bogner et al., 2012), rather than using the empirical distribution as was done in the original MCP method (Todini, 2008), an approximation of the discharge distribution is determined using a method similar to that presented in MacDonald et al. (2011). The approximation method applies kernel density estimation to the bulk of the distribution (Węglarczyk, 2018) and fits a Generalised type II Pareto Distribution (GPD) to the upper tail (Kleiber and Kotz, 2003) to create a composite distribution (see Fig. 2). The GPD is an extreme value distribution that is fully defined by three parameters: the location parameter a, the scale parameter b, and the shape parameter c. Within this composite distribution the location parameter also serves as the breakpoint which separates the kernel density and the GPD, and is shown in Fig. 2. The parameters of the GPD are determined using the concentrated likelihood method (see steps 4-6 below). The concentrated likelihood method allows the maximum likelihood estimates of multiple parameters to be determined by first

expressing one parameter in terms of the others (Takeshi, 1985). The time-series of discharge values, $\tilde{\boldsymbol{\eta}}(1:p) \in \mathbb{R}^p$, is used

260   here to described the distribution approximation which is implemented as follows:

1. All values in the time-series, $\tilde{\boldsymbol{\eta}}$, are sorted into descending order with $\tilde{\eta}_1$ denoting the largest value in the time-series, $\tilde{\eta}_2$ denoting the second largest value and so on.

2. A Gaussian kernel is centered at each data point such that

$$K_i(x) = \frac{1}{\sigma_{\tilde{\eta}}\sqrt{2\pi}} e^{-(x-\tilde{\eta}_i)^2/2\sigma_{\tilde{\eta}}^2} \tag{3}$$

265   where K_i is the kernel centered at $\tilde{\eta}_i$, and $\sigma_{\tilde{\eta}}$ is the Silverman's "rule of thumb" bandwidth (Silverman, 1984). The bandwidth is calculated using the in-built R function *bw.nrd0* (R Core Team, 2019; Venables and Ripley, 2002) and all values in the time-series, $\tilde{\boldsymbol{\eta}}$.

3. The kernel density is estimated using a leave-one-out approach such that the density at $\tilde{\eta}_j$ is

$$P(\tilde{\eta}_j) = \frac{1}{p-1}\sum_{i \neq j} K_i(\tilde{\eta}_j). \tag{4}$$

270   This makes sure the density is not over-fitted to any individual data point.

4. To guarantee data points in the tail, the largest 10 values are always assumed to be in the upper tail of the distribution (within the GPD) and the next 990 values (i.e. $\tilde{\eta}_{11}$ to $\tilde{\eta}_{1000}$) are each tried as the location parameter, a, of the GPD. If there are less than 1000 data points (i.e. $p < 1000$) then all data points are tried as the location parameter.

5. For each test value of a:

     i   The scale parameter, b, is determined analytically by the constraints that the density ~~must be consistent~~ distribution must be equal at the breakpoint ~~regardless of which of the two distributionsis used~~ for both the GPD and the KDE distributions, and the integral of the full density distribution function with respect to discharge must be equal to 1.

     ii   The shape parameter, c, is determined numerically by finding the maximum likelihood estimate, given the values of a and b, within the limits of $-1 \leq c \geq \frac{b}{\tilde{\eta}_1}$ (de Zea Bermudez and Kotz, 2010). The upper limit guarantees the upper bound of the distribution is greater than the maximum value in the time-series, $\tilde{\eta}_1$, and the lower limit constrains the number of values considered to reduce the computational time required. ~~The concentrated likelihood method is used (Takeshi, 1985).~~

     ~~This~~ For stations with $p > 1000$, this produces 990 sets of parameters.

6. ~~Of the sets of parameters found in step 5, maximum likelihood~~ The full distribution is the combination of the KDE and GPD weighted by their contribution to the total density, $F_{\tilde{\eta}}(a)$ and $1 - F_{\tilde{\eta}}(a)$, respectively (MacDonald et al., 2011). The likelihood function for the full distribution is used to ~~choose the~~ determine the maximum likelihood estimate of the location parameter, a, given the values of b and c that were calculated in step 5 for each possible value of a. This

results in the most likely set of parameters (a_{ML}, b_{ML}, c_{ML}) to define the GPD fitted to the upper tail of the distribution. ~~The likelihood function for the full distribution is the product of the likelihood function of the kernel density and the~~

290 ~~likelihood function of the GPD weighted by their contribution to the total density (MacDonald et al., 2011).~~

The six steps outlined above are applied separately to both the simulated time-series, $\tilde{\mathbf{s}}(1:p)$, and the observed time-series, $\tilde{\mathbf{y}}(1:p)$. Figure 2 illustrates the approximation method for the simulated discharge distribution for a single station.
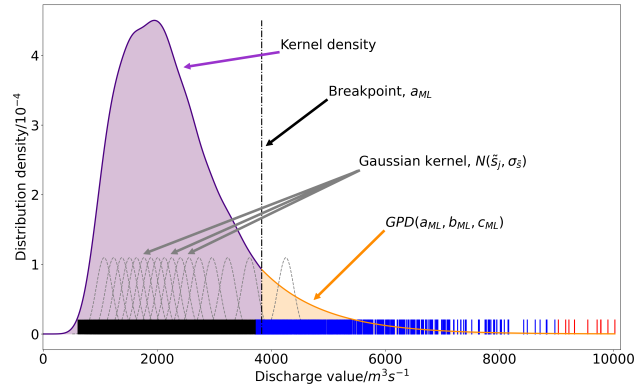
Figure 2. Schematic of the distribution approximation method. All data points are shown by the short solid lines. The largest 10 data points are red (always in the upper tail), the next 990 largest data points are blue (tried as the location parameter), and the remaining data points are black. Gaussian kernels (grey dashed lines) are used to calculate the kernel density (purple line). For clarity, only the kernels centered at every 500th data point are plotted. The upper tail is fitted with a Generalised type II Pareto distribution (orange line). The breakpoint (dot-dashed black line) defines the separation between the two distributions. The integral of the density distribution function with respect to discharge (the sum of the purple and orange shaded areas) equals 1.

Once the variables that define the discharge density distribution, namely $\sigma_{\tilde{\eta}}$, a_{ML}, b_{ML}, and c_{ML}, have been determined, the Cumulative Distribution Function (CDF) can be calculated analytically for both the observed and simulated discharge

295 distributions. All input data (for both the online and offline parts of the method) must be transformed to the standard Normal space using the NQT. However, it is too computationally expensive to calculate the analytical CDF for each data point. To increase the computational efficiency of the NQT, ~~both of the analytical~~ the KDE parts of the CDFs are approximated as piecewise linear functions. ~~The approximated CDFs are linear between knots (boundary points between pieces of the piecewise function) and can therefore be defined by the knots and the CDF values at the knots. The approximated CDFs are calculated~~

300 ~~separately for the observed and simulated distributions as follows:~~ Each data point in the historic time-series ~~, $\tilde{\eta}(1:p)$~~ is considered a knot ~~.~~ (a boundary point between pieces of the piecewise function). The CDF values at the mid-points between knots are approximated using linear interpolation ~~and compared to the analytical CDF values also calculated for the mid-points.~~ ~~.~~ If the approximated ~~CDF values at the midpoints are not within~~ and analytical CDFs differ by more than 1×10^{-5} ~~of the analytical CDF values~~ then the mid-points are added as additional knots. ~~Steps 2 and 3 are~~ The process is repeated until the

305 approximated CDF ~~values for all mid-points are within the allowed tolerance. The knots and the analytical CDF values at~~

the knots are saved in the station model. Within the NQT (described in Sect. 3.2) the CDF for any discharge value, $F_{\tilde{\eta}}(\tilde{\eta})$, is approximated by linearly interpolating between knots. is accurate to within 1×10^{-5}. Ensuring that the CDF for any discharge value can be determined using linear interpolation makes the application of the NQT more efficient.

3.3.2   Joint distribution estimation

310 This section describes the calculation of the joint distribution used in the online hydrological uncertainty estimation (see Sect. 3.4.1). First, the discharge distributions defined in Sect. 3.3.1 are used within the NQT to transform the historic observations and water balance simulation to the standard Normal space (see Fig. 1b). This allows the joint distribution to be calculated as a multivariate Gaussian distribution. The joint distribution is defined between the observations and water balance simulation values at L timesteps which, as noted in Sect. 3.1, is equal to the length of the recent period (q timesteps) and forecast period (T

315 timesteps) combined. The L timesteps are defined relative to a timestep k such that the joint distribution is a $2L$-dimensional distribution that describes the relationship between the observations, $\mathbf{y}(k-q+1:k+T)$, and the water balance simulation values, $\mathbf{s}(k-q+1:k+T)$. To ease notation we introduce the vector $\boldsymbol{\phi}(t_i:t_j)$, here defined generally for arbitrary timesteps, which includes the observed and simulated discharge values for all timesteps between timestep t_i and timestep t_j, such that

$$\boldsymbol{\phi}(t_i:t_j) = \begin{pmatrix} \mathbf{y}(t_i:t_j) \\ \mathbf{s}(t_i:t_j) \end{pmatrix}. \tag{5}$$

320 Following on from Eq. (5), we define the vector $\boldsymbol{\psi} \in \mathbb{R}^{2L}$

$$\boldsymbol{\psi}(k-q+1:k+T) = \begin{pmatrix} \boldsymbol{\phi}(k-q+1:k) \\ \boldsymbol{\phi}(k+1:k+T) \end{pmatrix} = \begin{pmatrix} \mathbf{y}(k-q+1:k) \\ \mathbf{s}(k-q+1:k) \\ \mathbf{y}(k+1:k+T) \\ \mathbf{s}(k+1:k+T) \end{pmatrix} \in \mathbb{R}^{2L}. \tag{6}$$

The splitting of the observed and simulated variables into two distinct time periods i.e. timesteps of $k-q+1$ to k and timesteps $k+1$ to $k+T$, is discussed below. The joint distribution can now be defined in terms of $\boldsymbol{\psi}(k-q+1:k+T)$.

The joint distribution is denoted $N_{2L}(\boldsymbol{\mu}_{\boldsymbol{\psi}}(k-q+1:k+T), \boldsymbol{\Sigma}_{\boldsymbol{\psi}\boldsymbol{\psi}}(k-q+1:k+T,k-q+1:k+T))$ where the subscript

325 $2L$ indicates its dimensions and the subscript $\boldsymbol{\psi}$ indicates that the distribution is for both observed and simulated variables for the two time periods shown in Eq. . The distribution is fully defined by its mean, $\boldsymbol{\mu}_{\boldsymbol{\psi}}(k-q+1:k+T) \in \mathbb{R}^{2L}$, and covariance matrix, $\boldsymbol{\Sigma}_{\boldsymbol{\psi}\boldsymbol{\psi}}(k-q+1:k+T,k-q+1:k+T) \in \mathbb{R}^{2L \times 2L}$. Since both the observed and simulated historic timeseries have been transformed into the standard Normal space the mean discharge value is zero for both distributions and therefore the mean vector is defined as $\boldsymbol{\mu}_{\boldsymbol{\psi}}(k-q+1:k+T) = \mathbf{0}$. The covariance matrix of the joint distribution is calculated using the historic

330 observations and water balance simulation as

$$\boldsymbol{\Sigma}_{\boldsymbol{\psi}\boldsymbol{\psi}}(k-q+1:k+T,k-q+1:k+T) = \frac{1}{p-L} \sum_{k=q}^{p-T} \boldsymbol{\psi}(k-q+1:k+T)\boldsymbol{\psi}(k-q+1:k+T)^T \in \mathbb{R}^{2L \times 2L}, \tag{7}$$

where $\psi(k-q+1:k+T)$ is defined as in Eq. (6) for each timestep, k, in the historic period. Since many stations have short time-series the impact of the seasonal cycle on the joint distribution is not considered. Additionally, any spurious correlations resulting from these short time-series are not currently treated.

335   To ensure that the covariance matrix, $\mathbf{\Sigma}_{\psi\psi}(k-q+1:k+T,k-q+1:k+T)$, is positive definite the minimum eigenvalue method is used (Tabeart et al., 2020). The covariance matrix is decomposed into the eigenvalues and eigenvectors. A minimum eigenvalue threshold is set as $1 \times 10^{-7}\lambda_1$, where λ_1 is the largest eigenvalue. All eigenvalues below this threshold are set to the threshold. The matrix is then reconstructed and scaled to match the variance of the original covariance matrix.

As mentioned, the joint distribution is used in the estimation of the hydrological uncertainty in the online part of the post-
340   processing method (see Sect. 3.4.1). If the joint-distribution is defined such that k is equal to the production time of a forecast then timesteps $k-q+1$ to k correspond to the recent period and timesteps $k+1$ to $k+T$ correspond to the forecast period. Therefore, the joint distribution can be used to condition the unknown observations and water balance simulation values in the forecast period on the known observations and water balance simulation values from the recent period. Here, we introduce notation that is used to split the joint distribution into the variables corresponding to ~~the recent period and the variables~~
345   ~~corresponding to the forecast period. Since the variables were split by timestep in the definition of $\psi(k-q+1:k+T)$~~each of these two periods. First, the mean vector ~~can also be~~ is split by timestep (as in Eq. (6)) such that

$$\boldsymbol{\mu}_\psi(k-q+1:k+T) = \begin{pmatrix} \boldsymbol{\mu}_\phi(k-q+1:k) \\ \boldsymbol{\mu}_\phi(k+1:k+T) \end{pmatrix}, \tag{8}$$

where ~~$\boldsymbol{\mu}_\phi(k-q+1:k)$ represents the mean of the variables in the recent period for a forecast produced at time k and $\boldsymbol{\mu}_\phi(k+1:k+T)$ represents the mean of the variables in the forecast period. The~~ the subscript ϕ indicates the distribution is
350   for the observed and simulated variables for a single time period, following the structure shown in Eq. (5), rather than for both time periods as indicated by the subscript ψ. The covariance matrix can be expressed as

$$\mathbf{\Sigma}_{\psi\psi}(k-q+1:k+T,k-q+1:k+T) = \begin{pmatrix} \mathbf{\Sigma}_{\phi\phi}(k-q+1:k,k-q+1:k) & \mathbf{\Sigma}_{\phi\phi}(k-q+1:k,k+1:k+T) \\ \mathbf{\Sigma}_{\phi\phi}(k+1:k+T,k-q+1:k) & \mathbf{\Sigma}_{\phi\phi}(k+1:k+T,k+1:k+T) \end{pmatrix}. \tag{9}$$

where $\mathbf{\Sigma}_{\phi\phi}(k-q+1:k,k-q+1:k)$ and $\mathbf{\Sigma}_{\phi\phi}(k+1:k+T,k+1:k+T)$ are the covariance matrices for variables in the recent and forecast periods, respectively, and $\mathbf{\Sigma}_{\phi\phi}(k-q+1:k,k+1:k+T)$ and $\mathbf{\Sigma}_{\phi\phi}(k+1:k+T,k-q+1:k)$ represent
355   the cross-covariance matrices of variables in both time periods.

These submatrices can be further decomposed into the components referring to the observed and the simulated variables such that, for example,

$$\mathbf{\Sigma}_{\phi\phi}(k+1:k+T,k+1:k+T) = \begin{pmatrix} \mathbf{\Sigma}_{\mathbf{yy}}(k+1:k+T,k+1:k+T) & \mathbf{\Sigma}_{\mathbf{ys}}(k+1:k+T,k+1:k+T) \\ \mathbf{\Sigma}_{\mathbf{sy}}(k+1:k+T,k+1:k+T) & \mathbf{\Sigma}_{\mathbf{ss}}(k+1:k+T,k+1:k+T) \end{pmatrix}, \tag{10}$$

where the subscripts $\mathbf{y}$ and $\mathbf{s}$ indicate that the distribution refers to the observed and simulated variables, respectively (in
360   contrast to the subscript ϕ which indicates both observed and simulated variables are included). The mean vector can also be

split in this way such that

$$\boldsymbol{\mu}_{\boldsymbol{\phi}}(k+1:k+T) = \left(\begin{array}{c} \boldsymbol{\mu}_{\mathbf{y}}(k+1:k+T) \\ \boldsymbol{\mu}_{\mathbf{s}}(k+1:k+T) \end{array} \right). \tag{11}$$

3.4 Online correction

This section describes the online correction part of the post-processing method (see Fig. 1c). The online correction quantifies
and combines the hydrological and meteorological uncertainties for a specific forecast to produce the final probabilistic fore-
cast. This forecast is produced at time t and has a maximum lead-time of T days, $\tilde{\mathbf{x}}_t(t+1:t+T) \in \mathbb{R}^{M \times T}$ (see Sect. 3.1 for
a description of the notation). As shown in Fig. 1, ~~the~~ as well as the current forecast produced at time t, the online correction
requires the following input data from the recent period:

- observations for the station, $\tilde{\mathbf{y}}(t-q+1:t) \in \mathbb{R}^q$

- the water balance simulation for the grid-box containing the station's location, $\tilde{\mathbf{s}}(t-q+1:t) \in \mathbb{R}^q$

- a set of ensemble streamflow forecasts (from the same system as the forecast $\tilde{\mathbf{x}}_t$) for the grid-box containing the station's
  location, $\{\tilde{\mathbf{x}}_{t-q+1}, \tilde{\mathbf{x}}_{t-q+2}, \ldots, \tilde{\mathbf{x}}_{t-1}\}$.

Previous work used tuning experiments to determine that a recent period of length 40 days (i.e. $q = 40$) was most appropriate
(Paul Smith, personal communication, September 2020). All the input data is transformed to the standard Normal space using
the NQT ~~therefore the tilde notation is not used in the following sections. The~~ (see Eq. (1)) and the CDFs determined in the
offline calibration (see Sect. 3.3) and stored in the station model, $F_{\tilde{y}}$ and $F_{\tilde{s}}$ ~~, are used in the NQT to transform the variables~~
~~as defined in Eq.~~. The observations are transformed using $F_{\tilde{y}}$, and the water balance simulation and forecasts are transformed
using $F_{\tilde{s}}$. The following sections provide more detail on the methods used to account for the uncertainties and are performed
within the standard Normal space. For simplicity, it is assumed that all data is available and there are no data latency issues such
that the most recent observation available is $\tilde{y}(t)$ for the timestep when the forecast is produced. In practice, some observations
from the recent period may not be available, and additionally the operational system does have data latency of approximately
1 day.

3.4.1 Hydrological uncertainties

The hydrological uncertainty is quantified using ~~an~~ a MCP method which uses the discharge values from the recent period
and the joint distribution, $N_{2L}(\boldsymbol{\mu}_{\boldsymbol{\psi}\boldsymbol{\psi}}, \boldsymbol{\Sigma}_{\boldsymbol{\psi}\boldsymbol{\psi}})$, defined in the offline calibration (see Sect. 3.3.2). The joint distribution defines
the relationship between the observations and water balance simulation across ~~L timesteps where, as stated in Sect. 3.1, L is~~
~~equal to the length of the recent period (q timesteps) and the forecast period (T timesteps) combined.~~ $L = q + T$ timesteps.
The hydrological uncertainty is estimated by conditioning the unknown observations and water balance simulation values in
the forecast period on the known observed and simulated discharge values from the recent period using the joint distribution.

390 First, the ~~station~~ observations and water balance simulations ~~for the station~~ from the recent period are combined into a single vector, $\boldsymbol{\phi}(t-q+1:t)$, as defined in Eq. (5).

In Sect. 3.3.2, the L timesteps of the joint distribution were defined relative to a timestep k. Here, k is set equal to the production time of the forecast, t, such that the timesteps from $t-q+1$ to t correspond to the recent period and the timesteps from $t+1$ to $t+T$ correspond to the forecast period. Thus, the mean vector of the joint distribution can be expressed, as

395 discussed in Sect. 3.3.2, as

$$\boldsymbol{\mu}_{\psi}(t-q+1:t+T) = \begin{pmatrix} \boldsymbol{\mu}_{\phi}(t-q+1:t) \\ \boldsymbol{\mu}_{\phi}(t+1:t+T) \end{pmatrix} \tag{12}$$

where $\boldsymbol{\mu}_{\phi}(t-q+1:t)$ represents the mean of the variables (both observations and water balance simulation) in the recent period, for which we have known values, $\boldsymbol{\phi}(t-q+1:t)$, and $\boldsymbol{\mu}_{\phi}(t+1:t+T)$ represents the mean of the variables in the forecast period, which we are required to predict.

400 The sub-matrices of the covariance matrix of the joint distribution that were defined in Eq. (10) are also positioned relative to timestep t, such that,

$$\boldsymbol{\Sigma}_{\psi\psi}(t-q+1:t+T,t-q+1:t+T) = \begin{pmatrix} \boldsymbol{\Sigma}_{\phi\phi}(t-q+1:t,t-q+1:t) & \boldsymbol{\Sigma}_{\phi\phi}(t-q+1:t,t+1:t+T) \\ \boldsymbol{\Sigma}_{\phi\phi}(t+1:t+T,t-q+1:t) & \boldsymbol{\Sigma}_{\phi\phi}(t+1:t+T,t+1:t+T) \end{pmatrix}. \tag{13}$$

By positioning the joint distribution in this way, $\boldsymbol{\mu}_{\phi}(t+1:t+T) \in \mathbb{R}^{2T}$ and the sub-matrix $\boldsymbol{\Sigma}_{\phi\phi}(t+1:t+T,t+1:t+T) \in \mathbb{R}^{2T \times 2T}$ create a climatological forecast for the observations and water balance simulation in the standard Normal space. It is

405 this climatological forecast that is conditioned on the discharge values from the recent period.

The conditional distribution of the unknown discharge values in the forecast period conditioned on the known discharge values in the recent ~~perion~~period, denoted $N_{2T}(\widehat{\boldsymbol{\mu}}_{\phi}(t+1:t+T),\widehat{\boldsymbol{\Sigma}}_{\phi\phi}(t+1:t+T,t+1:t+T))$, is calculated using the properties of a multivariate Gaussian joint distribution (Dey and Rao, 2006) such that

410 $\widehat{\boldsymbol{\mu}}_{\phi}(t+1:t+T) = \boldsymbol{\mu}_{\phi}(t+1:t+T)+$

$$\boldsymbol{\Sigma}_{\phi\phi}(t+1:t+T,t-q+1:t)\boldsymbol{\Sigma}_{\phi\phi}(t-q+1:t,t-q+1:t)^{-1}\Big(\boldsymbol{\phi}(t-q+1:t)-\boldsymbol{\mu}_{\phi}(t-q+1:t)\Big) \tag{14}$$

and

$\widehat{\boldsymbol{\Sigma}}_{\phi\phi}(t+1:t+T,t+1:t+T) = \boldsymbol{\Sigma}_{\phi\phi}(t+1:t+T,t+1:t+T)-$

415 $$\boldsymbol{\Sigma}_{\phi\phi}(t+1:t+T,t-q+1:t)\boldsymbol{\Sigma}_{\phi\phi}^{-1}(t-q+1:t,t-q+1:t)\boldsymbol{\Sigma}_{\phi\phi}(t-q+1:t,t+1:t+T). \tag{15}$$

where the hat notation indicates it is conditioned on the discharge values from the recent period.

The resulting predicted distribution, $N_{2T}(\widehat{\boldsymbol{\mu}}_{\phi}(t+1:t+T),\widehat{\boldsymbol{\Sigma}}_{\phi\phi}(t+1:t+T,t+1:t+T))$ is referred to as the *hydrological uncertainty distribution* and can be partitioned into two T-dimensional forecasts; one for the water balance simulation and one for the unknown observations in the forecast period such that,

$$
\begin{bmatrix} \mathbf{y}(t+1:t+T) \\ \mathbf{s}(t+1:t+T) \end{bmatrix} \sim N_{2T}\left(\begin{bmatrix} \widehat{\boldsymbol{\mu}}_{\mathbf{y}}(t+1:t+T) \\ \widehat{\boldsymbol{\mu}}_{\mathbf{s}}(t+1:t+T) \end{bmatrix}, \begin{bmatrix} \widehat{\boldsymbol{\Sigma}}_{\mathbf{yy}}(t+1:t+T,t+1:t+T) & \widehat{\boldsymbol{\Sigma}}_{\mathbf{ys}}(t+1:t+T,t+1:t+T) \\ \widehat{\boldsymbol{\Sigma}}_{\mathbf{sy}}(t+1:t+T,t+1:t+T) & \widehat{\boldsymbol{\Sigma}}_{\mathbf{ss}}(t+1:t+T,t+1:t+T) \end{bmatrix} \right).
$$

$$(16)$$

The subscripts $\mathbf{y}$ and $\mathbf{s}$ indicate that the distribution refers to the observed and simulated variables, respectively. ~~This notation was introduced in Sect. 3.3.2.~~

3.4.2 Meteorological uncertainty

425   This section describes the part of the online correction that estimates the meteorological uncertainty in the forecast of interest. As stated at the beginning of Sect. 3.4, the forecast of interest and the input data from the recent period are transformed into standard Normal space. The full transformed forecast, denoted by the forecast matrix $\mathbf{x}_t(t+1:t+T) \in \mathbb{R}^{T \times M}$ where each column represents an ensemble member (see Sect. 3.1), has ensemble mean $\overline{\mathbf{x}}_{\mathbf{t}}(t+1:t+T) \in \mathbb{R}^T$. The i-th component of $\overline{\mathbf{x}}_{\mathbf{t}}(t+1:t+T)$ represents the ensemble mean discharge at the i-th lead-time and is calculated as

430
$$
\overline{\mathbf{x}}_{\mathbf{t}}(t+1:t+T)[i] = \frac{1}{M} \sum_{m=1}^{M} \mathbf{x}_t(t+1:t+T)[i,m]
$$
$$(17)$$

The auto-covariance matrix of the forecast, $\boldsymbol{\Gamma}_{\boldsymbol{t}}(t+1:t+T,t+1:t+T) \in \mathbb{R}^{T \times T}$, is calculated such that the element corresponding to the i-th row and j-th column is given by

$$
\boldsymbol{\Gamma}_{\boldsymbol{t}}(t+1:t+T,t+1:t+T)[i,j] = \frac{1}{M-1} \sum_{m=1}^{M} (\mathbf{x}_t(t+1:t+T)[i,m] - \overline{\mathbf{x}}_{\mathbf{t}}(t+1:t+T)[i])(\mathbf{x}_t(t+1:t+T)[j,m] - \overline{\mathbf{x}}_{\mathbf{t}}(t+1:t+T)[j])^T.
$$

$$(18)$$

The uncertainty that propagates through from the meteorological forcings is partially captured by the spread of the ensemble
435   streamflow forecast. However, these forecasts are often under-spread particularly at shorter lead-times. The Ensemble Model Output Statistics method (EMOS, Gneiting et al., 2005) is used here to correct the spread only. Biases from the hydrological model are ignored in this section as the same hydrological model is used to create the water balance simulation and the forecasts. It is assumed that there is no bias in the meteorological forcings relative to the meteorological observations that are used to produce the water balance simulation (see Sect. 2) and that each ensemble member is equally likely. These assumptions
440   allow the value of the water balance simulation at any time k to be expressed as

$$
s(k) = \overline{\mathbf{x}}_l(k) + \epsilon
$$
$$(19)$$

where $\overline{\mathbf{x}}_i(k)$ is the ensemble mean for the timestep k of a forecast produced at time l (where $l+1 <= k <= l+T$), and ϵ is an unbiased Gaussian error. The value of the ensemble mean at timestep k, $\overline{\mathbf{x}}_l(k)$, is therefore a random variable from the distribution $N(s(k), \sigma_\epsilon^2)$.

The variance of ϵ, σ_ϵ^2, should equal the expected value of the spread of the forecast, $E[\mathbf{\Gamma_t}]$. However, this is not always satisfied. To correct the spread, a set of forecasts from the recent period are used to estimate two spread correction parameters. The corrected covariance matrix, $\mathbf{\Gamma_t^c}(t+1:t+T, t+1:t+T) \in \mathbb{R}^{T\times T}$, is then calculated, using these spread correction parameters, such that

$$\mathbf{\Gamma_t^c}(t+1:t+T, t+1:t+T) = \zeta\left(\delta\mathbf{I} + \mathbf{\Gamma_t}(t+1:t+T, t+1:t+T)\right) \tag{20}$$

where $\mathbf{I}$ is the identity matrix, and ζ and δ are the scalar spread correction parameters to be determined.

The ensemble mean at each lead-time and the auto-covariance matrices are calculated for each of the forecasts from the recent period after they have been transformed to the standard Normal space (not including the forecast produced at time t that is being corrected). Using the concentrated likelihood method (Takeshi, 1985) the spread correction parameters are defined as the maximum likelihoood estimates, ζ_{ML} and δ_{ML}, for the likelihood function

$$L(\zeta, \delta | \{\mathbf{x_{t-q+1}}, \ldots, \mathbf{x_{t-1}}\}) = \prod_{k=t-q+1}^{t-1} \frac{1}{\sqrt{2\pi\zeta(\delta\mathbf{I}+\mathbf{\Gamma_k})}} \exp\left(-\frac{1}{2\zeta(\delta\mathbf{I}+\mathbf{\Gamma_k})}(\overline{\mathbf{x}}_k - \mathbf{s})^2\right) \tag{21}$$

where we have used a shorthand notation for clarity, such that $\overline{\mathbf{x}}_k = \overline{\mathbf{x}}_k(k+1:k+T)$, $\mathbf{\Gamma_k} = \mathbf{\Gamma_k}(k+1:k+T, k+1:k+T)$, and $\mathbf{s} = \mathbf{s}(k+1:k+T)$ as defined above.

The current forecast, $\mathbf{x_t}(t+1:t+T)$, is spread-corrected to account for the meteorological uncertainty by applying the parameters, ζ_{ML} and δ_{ML}, as described in Eq. (20). This resultant distribution is referred to as the *meteorological uncertainty distribution* and provides a prediction of the water balance simulation in the forecast period, such that

$$\mathbf{s}(t+1:t+T) \sim N(\overline{\mathbf{x}_t}(t+1:t+T), \mathbf{\Gamma_t^c}(t+1:t+T, t+1:t+T)). \tag{22}$$

3.4.3 Combining uncertainties

The update step equations of the Kalman Filter (Kalman, 1960) are used to combine the hydrological and meteorological uncertainties to produce the final probabilistic forecast. The hydrological uncertainty distribution, defined in Eq. (16) and denoted $N_{2T}(\widehat{\boldsymbol{\mu}}_{\boldsymbol{\phi}}(t+1:t+T), \widehat{\boldsymbol{\Sigma}}_{\phi\phi}(t+1:t+T, t+1:t+T))$, is a predicted distribution for the water balance simulation and the observations during the forecast period. The meteorological uncertainty distribution, defined in Eq. (22) and denoted $N(\overline{\mathbf{x}_t}(t+1:t+T), \mathbf{\Gamma_t^c}(t+1:t+T, t+1:t+T))$, is a predicted distribution for the water balance simulation in the forecast period. The predictions of the distribution of the water balance are compared within the Kalman filter. In order to extract the water balance simulation part of the hydrological uncertainty distribution we define the matrix "observation operator" $\mathbf{H}$ such that

$$\widehat{\boldsymbol{\mu}}_\mathbf{s}(t+1:t+T) = \mathbf{H}\widehat{\boldsymbol{\mu}}_\psi(t+1:t+T) = \mathbf{H}\left(\begin{array}{c} \widehat{\boldsymbol{\mu}}_\mathbf{y}(t+1:t+T) \\ \widehat{\boldsymbol{\mu}}_\mathbf{s}(t+1:t+T) \end{array}\right) \in \mathbb{R}^T \tag{23}$$

where the subscripts $\mathbf{y}$ and $\mathbf{s}$ denote the observed and water balance simulation variables, respectively.

The update step of the Kalman filter is applied to produce a probabilistic forecast in the standard Normal space containing information about both the meteorological and hydrological uncertainties. The distribution of this forecast is denoted

$N_{2T}(\widehat{\boldsymbol{\mu}}_{\boldsymbol{\psi}}^{a}(t+1:t+T),\widehat{\boldsymbol{\Sigma}}_{\boldsymbol{\psi\psi}}^{a}(t+1:t+T,t+1:t+T))$, where the superscript a signifies the Kalman filter has been applied. The mean, $\widehat{\boldsymbol{\mu}}_{\boldsymbol{\psi}}^{a}(t+1:t+T))$, is calculated as

$$\widehat{\boldsymbol{\mu}}_{\boldsymbol{\psi}}^{a}(t+1:t+T) = \widehat{\boldsymbol{\mu}}_{\boldsymbol{\psi}}(t+1:t+T) + \mathbf{K}(\overline{\mathbf{x}}_{\mathbf{t}}(t+1:t+T) - \mathbf{H}\widehat{\boldsymbol{\mu}}_{\boldsymbol{\psi}}(t+1:t+T)) \tag{24}$$

where $\mathbf{K}$ is the Kalman gain matrix, defined as

$$\mathbf{K} = \widehat{\boldsymbol{\Sigma}}_{\boldsymbol{\psi\psi}}(t+1:t+T,t+1:t+T)\mathbf{H}^{\mathbf{T}}(\mathbf{H}\widehat{\boldsymbol{\Sigma}}_{\boldsymbol{\psi\psi}}(t+1:t+T,t+1:t+T)\mathbf{H}^{\mathbf{T}} + \boldsymbol{\Gamma}_{\boldsymbol{t}}^{\boldsymbol{c}}(t+1:t+T,t+1:t+T))^{-1}, \tag{25}$$

and $\mathbf{H}$ is the matrix observation operator defined above. The auto-covariance matrix is calculated as

$$\widehat{\boldsymbol{\Sigma}}_{\boldsymbol{\psi\psi}}^{a}(t+1:t+T,t+1:t+T) = (\mathbf{I} - \mathbf{KH})\widehat{\boldsymbol{\Sigma}}_{\boldsymbol{\psi\psi}}(t+1:t+T,t+1:t+T) \tag{26}$$

where $\mathbf{I}$ is the identity matrix and all other symbols are as before. The distribution produced by combining these two sources of uncertainty, $N_{2T}(\widehat{\boldsymbol{\mu}}_{\boldsymbol{\psi}}^{a}(t+1:t+T),\widehat{\boldsymbol{\Sigma}}_{\boldsymbol{\psi\psi}}^{a}(t+1:t+T,t+1:t+T))$, is for both the unknown observations and the water balance simulations variables in the forecast period. This distribution is partitioned into two T-dimensional forecasts which are in the standard Normal space such that

$$\begin{bmatrix} \mathbf{y}(t+1:t+T) \\ \mathbf{s}(t+1:t+T) \end{bmatrix} \sim N_{2T}\left(\begin{bmatrix} \widehat{\boldsymbol{\mu}}_{\mathbf{y}}^{a}(t+1:t+T) \\ \widehat{\boldsymbol{\mu}}_{\mathbf{s}}^{a}(t+1:t+T) \end{bmatrix}, \begin{bmatrix} \widehat{\boldsymbol{\Sigma}}_{\mathbf{yy}}^{a}(t+1:t+T,t+1:t+T) & \widehat{\boldsymbol{\Sigma}}_{\mathbf{ys}}^{a}(t+1:t+T,t+1:t+T) \\ \widehat{\boldsymbol{\Sigma}}_{\mathbf{sy}}^{a}(t+1:t+T,t+1:t+T) & \widehat{\boldsymbol{\Sigma}}_{\mathbf{ss}}^{a}(t+1:t+T,t+1:t+T) \end{bmatrix}\right) \tag{27}$$

where the subscripts $\mathbf{y}$ and $\mathbf{s}$ denote the observed and water balance simulation variables, respectively.

The T-dimensional distribution corresponding to the predicted distribution of the unknown observations in the forecast period, $N_{T}(\widehat{\boldsymbol{\mu}}_{\mathbf{y}}^{a}(t+1:t+T),\widehat{\boldsymbol{\Sigma}}_{\mathbf{yy}}^{a}(t+1:t+T,t+1:t+T))$, is transformed back into physical space using the inverse NQT, defined in Eq. (2), and the CDF of the observed discharge distribution, $F_{\tilde{y}}$. This forecast is then used to produce the 'real-time hydrograph' (see Fig. 4 for an example of this forecast product).

4 Evaluation strategy

4.1 Station selection

To maintain similarity with the operational system, the station models used in this evaluation are those calibrated for use in the operational post-processing. To avoid an unfair evaluation, station models must have been calibrated using observations from before the evaluation period. An evaluation period of approximately 2-years (from 1 January 2017 to 14 January 2019) was chosen to balance the length of the evaluation period with the number of stations evaluated. Of the 1200 stations post-processed operationally, 610 stations have calibration time-series with no overlap with the evaluation period. Additionally, stations were required to have at least 95% of the daily observations for the evaluation period ~~which reduced~~ reducing the number of stations

500 to ~~525, and a~~ 525. A further three stations were removed after a final quality control inspection (see Sect. 4.2.2 for details of
the observations and the quality control system used). The locations of the 522 stations are shown in Fig. 3. The marker colour
shows the CRPS of the raw ensemble forecast for a lead-time of 6 days. The spatial pattern of these CRPS values are discussed
in Sect. 5.1.4. Although all 522 stations are evaluated, specific stations (labelled in Fig. 3) are used to illustrate key results (see
Sect. 5.2). ~~These stations are labelled in Fig 3.~~
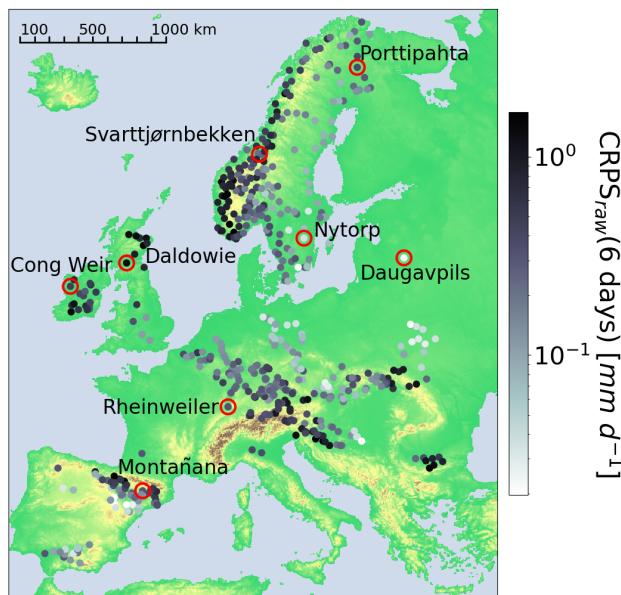
Figure 3. Map showing the locations of the 522 stations evaluated. The marker colour shows the Continuous Ranked Probability Score (see
Sect. 4.3.4) for the raw forecast at a lead-time of 6 days on a log scale. Perfect score: ~~CRPSS~~CRPS=0. Stations used as examples in Sect. 5
are labelled and highlighted by the red circles.

505 ## 4.2 Data

4.2.1 Reforecasts

~~In this study, reforecasts were used to evaluate the post-processing method. Reforecasts are forecasts for past dates created using a forecasting system as close to the operational system as possible (Hamill et al., 2006; Harrigan et al., 2020). As the EFAS system has recently been updated, using reforecasts allowed a larger number of forecasts to be evaluated.~~ The reforecasts

510 used in this study are a subset of the EFAS 4.0 reforecast dataset (Barnard et al., 2020). This dataset contains twice-weekly
reforecasts for dates that correspond to each Monday and Thursday in 2019. For example, 3 January 2019 is a Thursday, so
the dataset contains reforecasts for 3 January for every year from 1999 to 2018. The chosen evaluation period (see Sect. 4.1)
includes 208 reforecasts.

The raw forecasts were used as input for the post-processing method. Using twice-weekly reforecasts, rather than daily,

reduces the temporal correlations between forecasts and therefore limits the dependence of the results on the autocorrelation of the river discharge (Pappenberger et al., 2011). However, this means any single event cannot be included in the evaluation for all lead-times. For example, an event that occurs on a Saturday will not be included within the evaluation of the forecasts at a lead-time of 1 day which can only be a Tuesday or a Friday. Where necessary the evaluation metrics were combined over several lead-times (see Sects. 4.3.2 and 4.3.3). Additionally, fewer reforecasts were available to estimate the EMOS parameters in the meteorological uncertainty estimation (see Sect. 3.4.2). Whereas operationally ~~there would be 40 forecasts corresponding to the previous $q = 40$ days~~daily forecasts for each day of the recent period are available, here only ~~around 11 reforecasts were available within~~ two reforecasts are available for each week of the recent period. This reduces the number of forecasts used to estimate the EMOS parameters from 40 to 11. We did not extend the recent period to maintain consistency with the operational system and to avoid introducing errors due to any seasonal variation in the EMOS parameters.

~~Each reforecast is an ensemble forecast of 11 members created by forcing LISFLOOD with reforecasts from the ECMWF ensemble NWP system. At every timestep the mean discharge value for the previous 6 hours is predicted for each 5 km x 5 km grid-box in the EFAS domain. Currently~~ The reforecasts, and the operational forecasts (see Sect. 2), have a 6-hourly timestep. However, currently post-processing is ~~only performed for~~ performed at daily timesteps. Therefore, the reforecasts were aggregated to daily timesteps with a maximum lead-time of $T = 15$ days. ~~These ensemble reforecasts are henceforth referred to as the *raw forecasts*. The raw forecasts were used as input for the post-processing method to create the *post-processed forecasts*. Both sets of forecasts were evaluated as described in Sect. 4.3.~~

4.2.2 Observations

All discharge observations were provided by local and national authorities and collected by the Hydrological Data Collection Centre of the Copernicus Emergency Management Service and are the observations used operationally. The operational quality control process was applied to remove incorrect observations before they were used in this study (Arroyo and Montoya-Manzano, 2019; McMillan et al., 2012). Additionally, simple visual checks were performed to account for any computational errors introduced after the operational quality checks. Average daily discharge observations were used in three parts of the study. For each station, an historic time-series was used in the calibration of the station model (see Sect. 3.3). The length of the historic time-series, denoted p in Sect. 3.1, varies in length between stations. However, a minimum of 2-years of observational data between 1 January 1990 and 1 January 2017 is required. It should be noted that there is an overlap between the observations used for the calibration of the station models and the observations used for the calibration of the LISFLOOD hydrological model. For each reforecast, records of near real-time observations from the $q = 40$ days prior to the forecast time were used as the observations in the recent period (see Sect. 3.4.1). Observations from the evaluation period were used as the truth values in the evaluation (see Sect. 4.3).

 4.2.3 Water balance simulation

The EFAS 4.0 simulation (Mazzetti et al., 2020) was used as the water balance simulation for dates between 1 January 1990 and 14 January 2019. As described in Sect. 2, the water balance simulation is created by driving LISFLOOD with gridded meteorological observations. This dataset provides simulations for the whole of the EFAS domain. The values for the grid-boxes representing the locations of the stations were extracted creating a simulated time-series for each station. These time-series were aggregated from 6-hourly timesteps to daily timesteps (00 UTC to 00 UTC) and were used in three ways in this study. The water balance values for dates corresponding to the available observations in the historic period were used to calibrate the station model (see Sect. 3.3). For dates within the recent period for each reforecast, the water balance values were used in the post-processing (see Sect. 3.4.1). Finally, the water balance values corresponding to the 15 day lead-time of each reforecast was used to estimate the average meteorological error of each station (see Sect. 5.2.1).

4.3 Evaluation metrics

The evaluation of the post-processing method is performed by comparing the skill of the raw forecasts with the corresponding post-processed forecasts. Since the aim of the post-processing is to create a more accurate representation of the observation probability distribution all metrics use observations as the "truth" values. As mentioned in Sect. 2, the output from the post-processing method evaluated here is expressed operationally in the 'real-time hydrograph' product, an example of which is shown in Fig. 4. Therefore, the evaluation will consider four main features of forecast hydrographs.

4.3.1 Forecast median

In the real-time hydrograph the darkest shade of blue indicates the forecast median making it the easiest and most obvious single-valued summary of the full probabilistic forecast for end-users. The ensemble median of the raw forecasts is used in this evaluation because operationally the ensemble forecasts are often represented by boxplots where the median at each timestep is shown.

The skill of the forecast median is evaluated using the modified Kling-Gupta Efficiency score (KGE', Kling et al., 2012; Gupta et al., 2009). The forecast median is determined for the post-processed forecasts by extracting the 50th percentile of the probability distribution at each lead-time. For the raw forecasts the ensemble members are sorted by discharge value and the middle (i.e. 6th) member is chosen. This is done separately for each lead-time so the overall trajectory may not follow any single member. The forecast median is denoted x to distinguish it from the full forecast, $\mathbf{x_t}(t+1:t+T)$. The KGE' is calculated as,

$$KGE' = 1 - \sqrt{(r-1)^2 + (\beta-1)^2 + (\gamma-1)^2} \tag{28}$$

with

$$\beta = \frac{\overline{x}}{\overline{y}}, \tag{29}$$
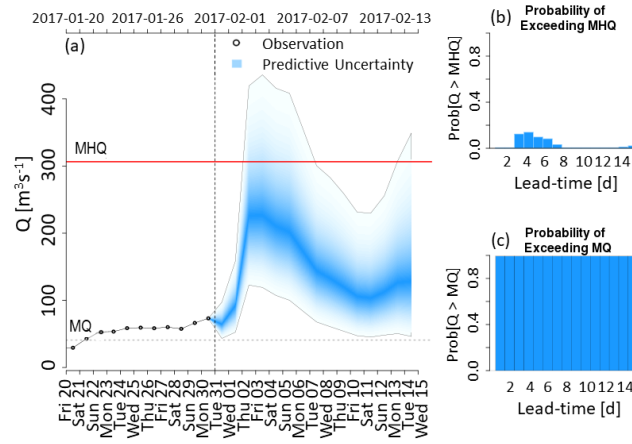
Figure 4. Example of the 'real-time hydrograph' product for the station in Brehy, Slovakia on 31 January 2017. (a) Probability distribution of the post-processed forecast. The darkest shade of blue indicates the forecast median (50th percentile) with each consecutive shade indicating a percentile difference such that the extent of the total predictive uncertainty is shown by the shaded region. Solid grey lines indicate the upper (99th percentile) and the lower (1st percentile) bounds of the forecast probability distribution. The red line shows the mean annual maximum (MHQ) threshold, and the dashed grey line shows the mean flow (MQ) threshold. Black circles represent observations positioned at the centre of the timestep over which they are calculated. (b) Bar chart showing the probability of the discharge exceeding the MHQ threshold at each lead-time. (c) Bar chart showing the probability of the discharge exceeding the MQ threshold at each lead-time.

and

$$\gamma = \frac{\sigma_x/\overline{x}}{\sigma_y/\overline{y}}, \tag{30}$$

where r is the Pearson's correlation coefficient, $\overline{x}$ and $\overline{y}$ are the mean values of the forecast median and the observations, respectively, and σ_x and σ_y are their standard deviations. The correlation, r, measures the linear relationship between the forecast median and the observations indicating the ability of the forecasts to describe the temporal fluctuations in the observations. The bias ratio, β, indicates if the forecast consistently under or over-predicts the observations. The variability ratio, γ, measures how well the forecast can capture the variability of the discharge magnitude. The KGE' is calculated separately for each lead-time. The KGE' ranges from $-\infty$ to 1, r ranges from -1 to 1, and both β and γ range from $-\infty$ to ∞. A perfect score for the KGE' and each of the components is 1.

4.3.2 Peak discharge

The timing of the peak discharge is an important variable of flood forecasts. The Peak-Time Error (PTE) is used to evaluate the effect of post-processing on the ~~ability of the forecast to predict the~~ timing of the peak within the forecast. The PTE requires a single-valued forecast trajectory. For the reasons stated in Sect. 4.3.1, the PTE is calculated using the forecast median, x. Peaks are defined as the maximum ~~value in the forecast period~~ forecast value and the PTE is calculated for forecasts where ~~the maximum observation~~ this peak exceeds the 90th percentile discharge threshold of the station. This threshold is calculated

using the full observational record for the station. The PTE is calculated as,

$$PTE = t_n^x - t_n^y \tag{31}$$

where t_n^x is the timestep of the maximum of the forecast median for the n-th forecast and t_n^y is the timestep of the maximum observed value in the same forecast period. A perfect score is $PTE = 0$. A negative PTE value indicates the peak is forecast too early and a positive PTE value indicates the peak is forecast too late. As the maximum lead-time is 15 days, the maximum value of the PTE is 14 days and the minimum value is -14 days.

4.3.3 Threshold exceedance

Two discharge thresholds are shown in the real-time hydrograph: the mean discharge (MQ) and the mean annual maximum discharge (MHQ). Both thresholds are determined using the observations from the historic period. For the post-processed forecasts, the probability of exceedance of the MQ threshold, $PoE(MQ)$, is calculated such that

$$PoE(MQ) = 1 - F_{\bar{x}}(MQ) \tag{32}$$

where $F_{\bar{x}}(MQ)$ is the value of the forecast CDF at the MQ threshold. The CDF is assumed to be linear between any two percentiles. The same method is applied for the MHQ threshold. For the ensemble forecast, each ensemble member above the threshold contributes one eleventh to the probability of the threshold being exceeded. The probability of the threshold being exceeded is calculated separately for each lead-time.

The Relative Operating Characteristic (ROC) score and ROC diagram (Mason and Graham, 1999) are used to evaluate the potential usefulness of the forecasts with respect to these two thresholds. The ROC diagram shows the probability of detection vs the false alarm rate for alert trigger thresholds from 0.05 to 0.95 in increments of 0.1. The ROC score is the area below this curve with a ROC score of less than 0.5 indicating a forecast with less skill than a climatological forecast. As discharge values of above the MHQ threshold are rare, all stations are combined and lead-times are combined into 3 groups; 1-5 days, 6-10 days, and 11-15 days. Since the reforecasts are only produced on Monday and Thursdays, an event that occurs on a Saturday can only be forecasted at lead-times of 2, 5, 9, and 12 days. Using 5-day groupings of lead-times guarantees that each group is evaluated against each event at least once but allows the usefulness of the forecasts to be compared at different lead-times. A perfect forecasting system would have a ROC score of 1.

Reliability diagrams are used to evaluate the reliability of the forecast in predicting the exceedance of the two thresholds. Reliability diagrams show the observed frequency vs the forecast probability for bins of width 0.1 from 0.05 to 0.95. A perfectly reliable forecast would follow the one-to-one diagonal on a reliability diagram. The same combination of stations and lead-times is used as with the ROC diagrams.

4.3.4 Full probability distribution

A commonly used metric to evaluate overall performance of a probabilistic or ensemble forecast is the Continuous Ranked Probability Score (CRPS, Hersbach, 2000). The CRPS measures the difference between the CDF of the forecast and that of

the observation and is defined as

$$CRPS\left(F_{\tilde{x}}, y\right) = \int_{-\infty}^{\infty} \left(F_{\tilde{x}}\left(\tilde{\eta}\right) - \theta\left(\tilde{\eta} - y\right)\right)^2 d\tilde{\eta} \tag{33}$$

where $F_{\tilde{x}}$ represents the CDF of the forecast and $\theta(\tilde{\eta} - y)$ is the step function (Abramowitz and Stegun, 1972), defined such that

$$\theta(\tilde{\eta}) = \begin{cases} 0 & \tilde{\eta} < 0 \\ 1 & \tilde{\eta} \geq 0 \end{cases} \tag{34}$$

and represents the CDF of the observation, y. The post-processed forecasts are defined via their percentiles, therefore by assuming the CDF is linear between percentiles the CRPS can be calculated directly. The empirical CDF of the raw forecasts, defined via point statistics, is used and the CRPS is calculated using a computationally efficient form (Jordan et al., 2019, Equation 3). It should be noted that the error in the calculation of the CRPS for the raw ensemble forecasts is likely to be large compared to that of the post-processed forecasts because of the limited number of ensemble members (Zamo and Naveau, 2018). However, as this evaluation is of the post-processing method no corrections to account for the ensemble size are made (e.g. Ferro et al., 2008) since the impact of the post-processing would be difficult to differentiate from that of the CRPS correction. The CRPS ranges from a perfect score of 0 to ∞.

4.3.5 Comparison

For some of the metrics described in Sects. 4.3.1-4.3.4, the impact of post-processing is shown using the respective skill score, SS, with the raw forecast as the benchmark,

$$SS = \frac{S_{pp} - S_{raw}}{S_{perf} - S_{raw}} \tag{35}$$

where S_{pp} and S_{raw} are the scores for the post-processed forecast and the raw forecast, respectively, and S_{perf} is the value of the score for a perfect forecast. The skill score gives the fraction of the gain in skill required for the raw forecast to become a perfect forecast that is provided by the post-processing. A value $SS < 0$ means the forecast has been degraded by the post-processing, a value of $SS > 0$ indicates that the forecast has been improved by the post-processing, and a value of $SS = 1$ means that the post-processed forecast is perfect. Henceforth, the skill score for a metric is denoted by adding 'SS' to the metric name.

5 Results and Discussion

5.1 Performance of the post-processing method

This section focuses on the overall impact of post-processing at all 522 of the evaluated stations across the EFAS domain and aims to address the research question: *Does the post-processing method provide improved forecasts?*

5.1.1 Forecast median

The modified Kling-Gupta Efficiency Skill Score (KGESS) is used to evaluate the impact of post-processing on the forecast median (see Sect. 4.3.1). Figure 5a shows the KGESS for all stations at every other lead-time such that each boxen plot (also known as letter-value plots, Hofmann et al., 2017) contains 522 values, one for each station. For each lead-time the central black line shows the median KGESS value. The inner box (the widest box) represents the interquartile range and contains 50% of the data points. Each subsequent layer of boxes splits the remaining data points in half such that the second layer of boxes are bounded by the 12.5th and 87.5th percentiles and contains 25% of the data points. The outliers represent a total of 2% of the most extreme data points. The lower panels of Fig. 5 show the three components of the KGE' (b: correlation, c: bias ratio, d: variability ratio) for lead-times of 3, 6, 10, and 15 days for all stations for both the raw forecasts (orange) and the post-processed forecasts (purple). The chosen lead-times are representative of the results.
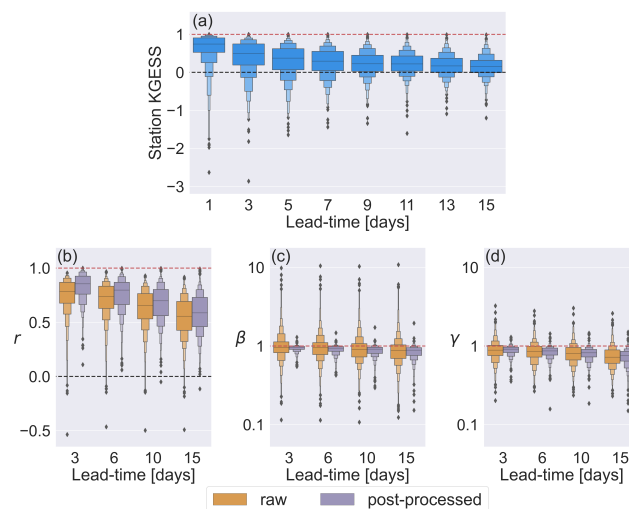
Figure 5. Comparison of the raw and post-processed forecast medians. (a) The Kling-Gupta Efficiency Skill Score (KGESS) for the forecast medians at all 522 stations for every other lead-time. Red dashed line shows the perfect score of KGESS = 1. Black dashed lines show KGESS value of 0. KGESS > 0 indicates the skill of the forecast median is improved by post-processing. KGESS < 0 indicates the skill of the forecast median is degraded by post-processing. The three components of the KGE': (b) Correlation component, r. Black dashed line shows r = 0. (c) Bias ratio component, β. (d). Variability ratio component, γ. Red dashed lines show the perfect scores of 1 for all components. Both (c) and (d) have logarithmic y-axes.

Figure 5a shows that most stations have positive KGESS values at all lead-times indicating that post-processing increases the skill of the forecast median. However, the magnitude of this improvement decreases at longer lead-times . The median KGESS value decreases from 0.75 at a lead-time of 1 day to 0.15 at a lead-time of 15 days with most of this the reduction occurring in the first 7 days. Nonetheless, over 11% of stations have a KGESS greater than 0.5 at a lead-time of 15 days; most notably the station in Nytorp, Sweden has a KGESS above 0.98 at this lead-time. As discussed in Sect. 5.2.2, the large KGESS values at the Nytorp station are due to the correction of a large bias in the raw forecast. The proportion of stations for which

post-processing degrades the forecast median increases with lead-time ~~from 8% at 1 day to 26% at 15 days.~~ However, the lowest KGESS values become less extreme (i.e. not as negative). This increase in the KGESS of the most degraded stations is due to a decrease at longer lead-times in the skill of the raw forecast (used as the benchmark for the skill score) rather than an increase in the skill of the post-processed forecasts. This shows that the effect of naïve skill on the results should be considered; however, as the aim is to evaluate the impact of post-processing, it is appropriate to use the raw forecasts as the benchmark (Pappenberger et al., 2015b).

Figure 5b shows ~~the correlation component, r, of the KGE' for both the raw and the post-processed forecast medians. Post-processing~~ that post-processing improves the correlation between the forecast median and the observations for most stations, particularly at short lead-times ~~where approximately 30% of stations have an improved correlation of over 0.1. However, at longer lead-times almost 40% of stations show a decrease in correlation with the observations and 10% show a decrease of more than 0.1 for at least one lead-time.~~ The impact of post-processing on the correlation component of the KGE' varies greatly between stations. Notably, the flashiness of the catchment and whether or not the river is regulated can affect the performance of the post-processing (see Sect. 5.2.2). Additionally, the quality and length of the calibration time-series also have an effect (see Sect. 5.2.3).

Figure 5c shows the bias ratio, β, which indicates if on average the forecasts over or under-estimate the discharge at a station. ~~The post-processing method attempts to correct for any consistent hydrological biases (differences between the observations and the water balance simulation) during the~~ In the hydrological uncertainty estimation part of the online correction (see Sect. 3.4.1) ~~. The climatological discharge distribution is conditioned on the discharge values from the recent period. The~~ the mean of the ~~conditioned~~ hydrological uncertainty distribution is calculated in Eq. (14) as the mean flow of the observed time-series from the historic period (term 1) plus an amount dependent on the discharge values in the recent period (term 2). Therefore, assuming the mean flow does not change between the calibration (historic) and evaluation periods, any consistent biases in the hydrological model climatology should be corrected.

Figure 5c shows the variability ratio, γ, which indicates if the forecast median is able to capture the variability of the flow. In general, the post-processing method does ~~succeed in bias correcting the forecasts~~ reduces the bias in the forecast median. For raw forecasts, the β-values range from approximately 10 (an over-estimation by an order of magnitude) to 0.1 (an under-estimation of an order of magnitude) ~~with an almost equal split between over and under-estimation at short lead-times, and a tendency towards under-estimation at longer lead-times.~~ For the post-processed forecasts the β-values are more tightly clustered around the perfect value of $\beta = 1$. The largest improvements to the β-values are for stations where the flow is under-estimated by the raw forecasts. ~~This is because many of the~~ Some stations with raw β-values of greater than 1 are over-corrected such that the post-processed forecasts have β-values of less than 1. This is supported by the similarity of the median β-values for the raw and post-processed forecasts despite the decrease in the range of values. For stations where the over-estimation by the raw forecast is relatively small the over-correction can result in the post-processed forecasts being more biased than the raw forecasts. The over-correction is generally due to the under-estimation of high flows (see discussion on the third component of the KGE', the variability ratio) which results in an under-estimation of the average flow and hence a β-value of less than 1. ~~For stations where the raw forecast largely over-estimates the discharge, this over-correction is not sufficient to cause a~~

There is a small decrease in the β-values at longer lead-times for both the raw and post-processed forecasts. This is primarily caused by an increase in the under-estimation of high flows at longer lead-times as the skill of the forecast decreases. However, for some stations the drift in β-values at longer lead-times is also caused by nonstationarity of the discharge distribution. A change in the discharge distribution from that of the calibration period means the hydrological uncertainty is calculated using an inaccurate climatological mean (term 1 of Eq. (14)). The impact of the discharge values from the recent period (term 2 of Eq. (14)) decreases with lead-time because the autocorrelation weakens. Therefore, any errors in the climatological forecast are more pronounced at longer lead-times.

Figure 5d shows that the variability of the flow tends to be under-estimated by the raw forecast (γ less than 1). The under-estimation is because the magnitudes of the peaks relative to the mean flow are not predicted accurately particularly at longer lead-times. This decrease in γ-values at longer lead-times is also visible for the post-processed forecasts. However, at all lead-times most stations show an improvement after post-processing (i.e. have a value of γ closer to 1). Stations where the raw forecast over-estimates the variability (γ above 1) are more likely to have the variability corrected by post-processing particularly at longer lead-times.

The two factors impacting the ability of the post-processed forecasts to capture the variability of the flow are 1) the level of indication of the upcoming flow by the discharge values in the recent period, and 2) the spread of the raw forecast. In the Kalman filter when the hydrological uncertainty distribution and the meteorological uncertainty distribution are combined (see Sect. 3.4.3) the weighting of each distribution is dependent on their relative spreads. The spread of the hydrological uncertainty is impacted by the discharge values in the recent period. Due to the skewedness of discharge distributions, the climatological forecasts tend to have a low probability of high flows. If the recent discharge values show no indication of an upcoming high flow (i.e. no increase in discharge), the low probability of high flows is reenforced. This decreases the spread of the hydrological uncertainty distribution and increases its weight within in the Kalman filter.

The meteorological uncertainty distribution is the spread corrected raw forecast and includes the variability due to the meteorological forcings. For floods with meteorological drivers, if the magnitude of the peaks is under-predicted by the raw forecasts then the post-processed forecasts are also likely to under-predict the magnitude of the peaks. Alternatively, if the raw forecast is unconfident in the prediction of a peak (e.g. only a couple of members predict a peak) then it may not have a
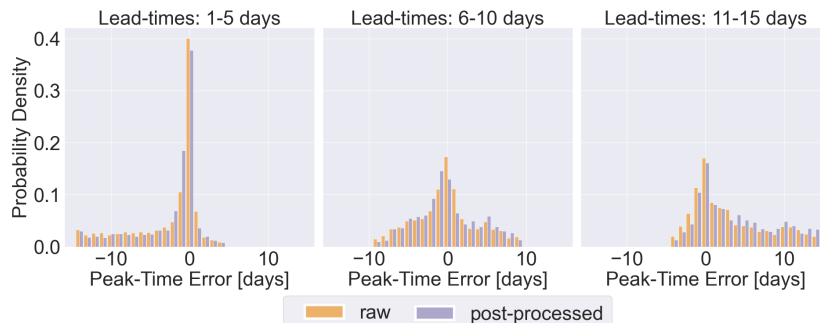
Figure 6. Histograms showing the probability distribution of Peak-Time Errors for all forecasts where the maximum observation is above the 90% percentile for the station (26807 forecasts) for raw forecasts (orange) and post-processed forecasts (purple). (a) Maximum observations occurs on lead-times of 1 to 5 days. (b) Maximum observations occurs on lead-times of 6 to 10 days. (c) Maximum observations occurs on lead-times of 10 to 15 days.

sufficient impact within the Kalman filter and the post-processed forecast may not predict the peak regardless of the accuracy of the ensemble members that do predict the peak. The impact of the spread correction is discussed further in Sect. 5.2.1.

735   The ensemble mean is another commonly used single-valued summary of an ensemble forecast (Gneiting, 2011). Although the comparison presented here uses the ensemble median we also show the three components of the KGE' for the ensemble mean in Fig. 1 of the supplementary material. The ensemble means (see Fig. 1b of the supplementary material) do not show the general drift in β-values with increasing lead-time that is discussed above for both the ensemble median and post-processed forecasts. However, the range of β-values is similarly large for both the ensemble median and the ensemble mean. In terms of

740   the correlation coefficient and the variability ratio the ensemble mean performs similarly or worse than the ensemble median (see Fig. 1a and 1c of the supplementary material, respectively).

5.1.2   Timing of the peak discharge

To evaluate the impact of post-processing on the ability of the forecast to predict the timing of the peak flow accurately the Peak-Time Error (PTE, see Sect. 4.3.2) is used. The aim of this assessment is to see how well the forecast is able to identify

745   the time within the forecast period with highest flow and therefore greatest hazard. A PTE of less than 0 indicates the peak is predicted too early whereas a PTE of greater than 0 indicates the peak was predicted too late. Figure 6 shows the distribution of the PTE values for both the post-processed and raw forecasts for all forecasts where the maximum ~~observed value in the forecast period~~ forecast value exceeds the 90th percentile ~~within the forecast period~~. The forecasts are split into three categories dependent on the lead-time at which the ~~observed~~ forecast maximum occurs. Therefore, the distributions shown in each panel

750   are truncated at different values of PTE. For example, ~~an observation occurring~~ if the forecast maximum occurs on a lead-time between 1 and 5 days, it can at most be predicted 5 days early.

     Approximately ~~50~~40% of the forecast medians of the raw forecasts have no error in the timing of the peak for peaks that occur within lead-times of 1 to 5 days. This drops to ~~40~~37% for post-processed forecasts. Both sets of forecasts have approximately

~~70~~60% of forecasts with timing errors of 1 day or less. However, the post-processed forecasts ~~tend to predict the peak too early whereas the raw forecasts are approximately equally split between predicting peaks too early and too late. Although~~ are more likely to ~~correctly predict the timing of the peak , raw forecasts are also more likely than the post-processed forecasts to have larger PTE values indicating the peak is predicted several days too late~~predict the peak too early. For maximum ~~observed~~ forecast values occurring on lead-times of 6 to 10 days, the post-processed forecasts still tend to predict peaks earlier than the raw forecasts~~but are also more likely to predict the peak several days too late. For maximum observed values occurring at the longest~~. However, for maximum forecast values occurring on lead-times of ~~10~~11 to 15 days the post-processed forecasts are ~~slightly~~ more likely to predict the ~~timing of the peak correctly. However, they are also more likely to predict the peak~~ peaks several days too late. ~~The distribution of PTE values is bimodal for both sets of forecasts with a peak at $PTE = 0$ and a peak at $PTE = -14$. This is usually due to the underestimation of the discharge at~~ This suggests that for floods forecast at longer lead-times by the ~~forecast median for forecasts that are preceded by high flows in the recent period resulting in high initial conditions~~post-processing forecasts should be considered carefully.

Overall the impact of post-processing is small but tends towards the early prediction of the peak flow for short lead-times and late peak predictions for longer lead-times. However, there are three main limitations with this analysis. The first is that both sets of forecasts are probabilistic and therefore the median may not provide an adequate summary of the forecast. ~~To account for the probability distribution, this analysis was repeated for the lowest and highest percentiles (not shown). For the raw forecasts the lowest and highest ensemble members at each lead-time were used and for the post-processed forecasts the 1st and 99th percentiles were used (solid grey lines in Fig. 4). For both the lowest and highest percentiles the post-processed forecasts are more likely to predict the peak earlier (and usually too early) than the raw forecast regardless of lead-time.~~

Secondly, the evaluation here is forecast-based rather than peak-based in that the focus is the timing of the highest discharge value in the forecast within the forecast period and not the lead-time at which a specific peak is predicted accurately. This was intentional as the twice-weekly production of the reforecasts means that a specific peak does not occur at each lead-time.

Finally, the combination of forecasts at all stations means the relationship between the runoff generating mechanisms and the PTE cannot be assessed. ~~It was found that although in general the post-processed forecasts predict the timing of the peak less accurately (too early), this degradation to the timing of the peak was more common if the maximum observation was surrounded by relatively low observations than if the discharge was high for a longer period (not shown). The impact of slow and fast catchment responses is discussed in more detail in Sect. 5.2.2.~~

5.1.3 Threshold exceedance

The Relative Operating Characteristic (ROC) diagrams for the mean flow (MQ) and the mean annual maximum flow (MHQ) thresholds (see Sect. 4.3.3) are shown in Fig. 7. The diagrams show the probability of detection against the false alarm rate for varying decision thresholds. The forecast period is split into three lead-time groups: 1-5 days, 6-10 days, and 11-15 days (see Sect. 4.3.3). The ROC scores for the MQ and MHQ thresholds are given in Table 1 for each lead-time group for the raw and post-processed forecasts, along with the corresponding skill scores (ROCSS). Both the raw and post-processed forecasts have ROC scores greater than 0.5 showing that they are more skilful than a climatological forecast.
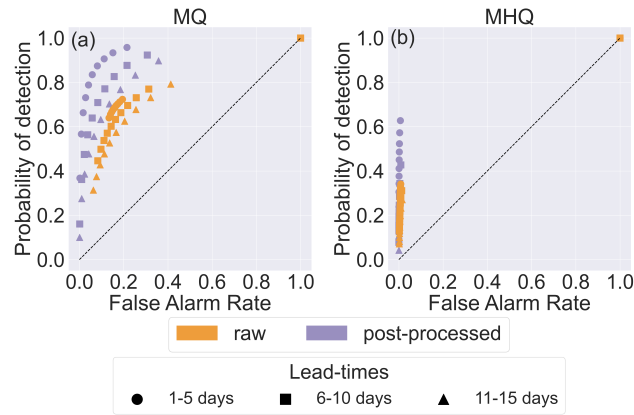
Figure 7. Relative Operating Characteristic diagrams for (a) the MQ threshold (118,888 observations above MQ), and (b) the MHQ threshold (2783 observations above MHQ). All stations are combined and groupings of lead-times are used (see Sect. 4.3.3.)

The spread of the raw forecasts is small at short lead-times. This is shown by the overlapping of the points in Fig. 7a for lead-times of 1-5 days (orange circles). The similarity of the points indicates that the decision thresholds are usually triggered simultaneously and therefore that the forecast distribution is narrow. The spread of the forecast increases with lead-time as the ensemble of meteorological forcings increases the uncertainty in the forecasts. Although the skill of the forecast median decreases with lead-time (see Sect. 5.1.1), the introduction of the meteorological uncertainty means the usefulness of the raw forecasts is similar for lead-times of 1-5 days and 6-10 days. This is shown by similarity of the ROC scores for these lead-time groups for the raw forecast.

Post-processing also accounts for the hydrological uncertainty allowing for a more complete representation of the total predictive uncertainty. In addition, as shown in Fig. 5c, post-processing bias corrects the forecast relatively well at short lead-times. The combination of spread and bias correction leads to an increase in the probability of detection for all but the highest decision thresholds and a decrease in the false alarm rate for almost all decision thresholds and lead-times. The added reliability gained from post-processing decreases with lead-time. The ROCSS for lead-times of 1-5 days at the MQ level is 0.8 but is only 0.45 for lead-times of 11-15 days.

The ROC diagram for the MHQ threshold (Fig. 7b) shows that the raw forecasts tend to cautiously predict high flows with the forecast much more likely to miss a flood than to issue a false alarm even for the lowest decision threshold. There is less improvement from post-processing than for the MQ threshold with the ROCSS for the MHQ threshold only reaching 0.48 for 1-5 days lead-time. For the MHQ threshold, the post-processing increases the probability of detection and decreases the false alarm rate at short lead-times. At longer lead-times the false alarm rate is still decreased by post-processing, but the probability of detection is also decreased for the largest decision thresholds. This reluctance to forecast larger probabilities also occurs with the MQ threshold and is due to the interaction between the hydrological and meteorological uncertainty in the Kalman filter discussed in Sect. 5.1.1.

	MQ			MHQ		
Lead-time	ROCraw	ROC$_{pp}$	ROCSS	ROCraw	ROC$_{pp}$	ROCSS
1-5 days	0.78	0.96	0.87	0.68	0.83	0.48
6-10 days	0.78	0.91	0.56	0.68	0.74	0.20
11-15 days	0.76	0.87	0.45	0.67	0.69	0.08

Table 1. Relative Operating Characteristic Scores (ROCS) and corresponding skill scores (ROCSS) for the raw and post-processed (pp) forecasts for lead-times of 1-5 days, 6-10 days, and 10-15 days for the mean flow threshold (MQ) and the mean annual maximum threshold (MHQ).

Figure 8 shows reliability diagrams for the MQ and MHQ thresholds. For the MQ threshold (Fig. 8a) the raw forecasts are
810   over-confident leading to under-estimation of low probabilities and over-estimation of high probabilities. The post-processed forecasts are more reliable but also tend to under-estimate low probabilities. The raw forecasts increase in reliability with lead-time whereas the reliability of the post-processed forecasts decreases. This is also true for the MHQ threshold.
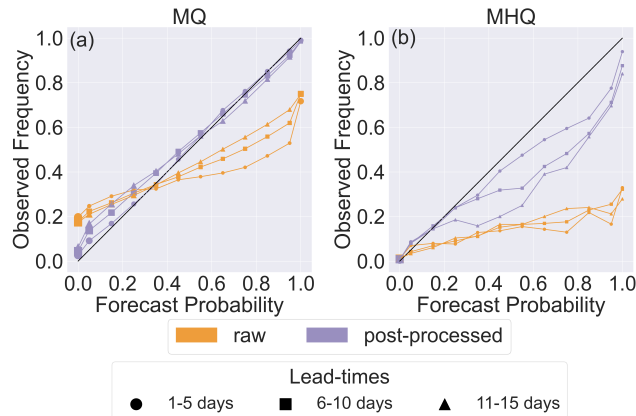
Figure 8. Reliability diagrams for (a) the mean flow threshold (MQ), and (b) the mean annual maximum flow (MHQ). All stations are combined and groupings of lead-times are used (see Sect. 4.3.3.)

Both sets of forecasts are consistently below the diagonal in the MHQ reliability diagram (Fig. 8b) indicating unconditional biases. However, the post-processed forecasts have smaller biases consistent with the results discussed in Sect. 5.1.1. In addi-
815   tion, the raw forecast shows relatively poor resolution with events occurring at approximately the same frequency regardless of the forecast probability.

The distribution of forecasts (shown by marker size) is more uniform for the post-processed forecasts particularly at shorter lead-times. Since the ensemble reforecasts evaluated have 11 members and the operational forecasts have 73 members, the distribution for operational raw forecasts is expected to be slightly more even as the additional members allow for greater

 gradation in the probability distribution. The distribution of forecasts is skewed towards low probabilities showing similarly to the ROC diagrams (Fig. 7) that both sets of forecasts tend to cautiously forecast flows exceeding the MHQ threshold.

5.1.4 Overall skill

The Continuous Ranked Probability Skill Score (CRPSS) is used to evaluate the impact of post-processing on the overall skill of the probability distribution of the forecasts. Figure 9 shows the CRPSS for each station at lead-times of 3, 6, 10, and 15 days. Stations that are degraded by post-processing (CRPSS < 0) are circled in red. Stations that show a large increase in skill after post-processing (CRPSS > 0.9) are circled in cyan.
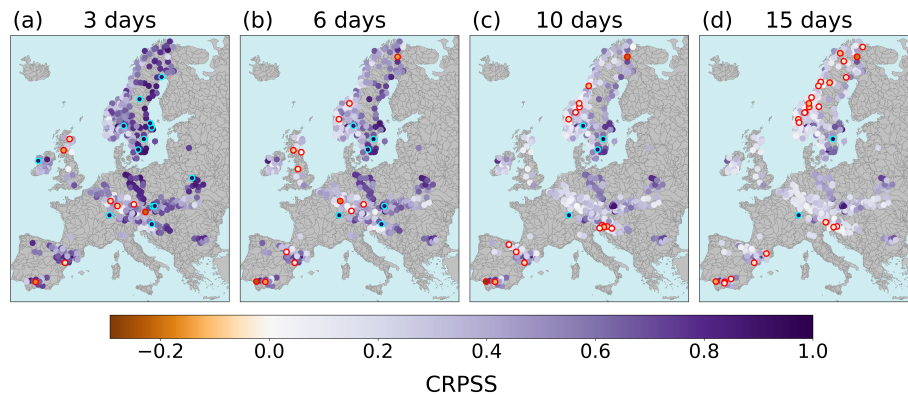
Figure 9. The Continuous Ranked Probability Skill Score (CRPSS) for all 522 stations for lead-times of 3, 6, 10, and 15 days. CRPSS values below 0 indicate the forecast probability distribution is on average less skillful after post-processing and values above 0 indicate added skill after post-processing. Markers are outlined in red if the CRPSS is below 0 and in cyan if the CRPSS is above 0.9.

As was seen with the KGESS for the forecast median, there is a decrease in the improvement offered by post-processing at longer lead-times. This can be seen in Fig. 9, by the gradual change from dark purple to light purple/white values for panels (a) to (d). It is also shown in the increase of red circles and the decrease of cyan circles. Approximately 55% of stations have a CRPSS of above 0.5 at a lead-time of 3 days and this decreases to 10% by a lead-time of 15 days. At a lead-time of 3 days, 8 stations are degraded by the post-processing and 13 stations have a CRPSS greater than 0.9. By a lead-time of 15 days these change to 24 degraded stations and only 2 stations with CRPSS values greater than 0.9. Many of the stations that are improved significantly have large hydrological biases. For example, one of the most improved stations at a lead-time of 15 days is in Rheinweiler, Germany (see Fig. 3) which has a large bias in the hydrological model output due to limitations in the representation of the drainage network in the model domain. The post-processing method can account for these biases (see Sect. 5.1.1) resulting in CRPSS values greater than 0.9 at all lead-times.

The lack of clustering of the stations with CRPSS values above 0.9 suggest that the magnitudes of the largest corrections are due to station dependent characteristic. On the other hand, the degraded stations at a lead-time of 3 days appear to cluster in three loose regions. In all three regions the degradation is due to high short-duration peaks being captured better by the raw

840   forecasts than the post-processed forecasts. At longer lead-times the Spanish catchments are still degraded but the Scottish stations are not. As discussed in Sect. 5.1.1 for the lowest KGESS values, this is due to a decrease in the skill of the raw forecasts. The degraded stations at lead-times of 10 and 15 days cluster in Spain, around the Kjolen Mountains, and in the Sava catchment. The poorly post-processed forecasts in the Sava catchment are downstream of a reservoir the impact of which is discussed in Sect. 5.2.2.

845   Comparing the CRPSS values in Fig. 9 with the raw CRPS values shown in Fig. 3 shows similarities in the spatial pattern of the raw forecast skill and the spatial pattern of the magnitude of improvement due to post-processing. In general, stations with low CRPS scores (high skill) for the raw forecasts are improved the most by post-processing. For example, the west coast of the Scandinavian Peninsula has a lower raw skill in general and the level of improvement is also lower than that of the east coast. However, there are some anomalies to this pattern. For example, the station in Cong Weir, Ireland has a relatively low

850   raw forecast skill compared to surrounding catchments due to regulation of the streamflow but has a high CRPSS value at all lead-times~~(over 0.9 at 3 days)~~. Additionally, whilst stations on the River Rhine and the River Oder have similar raw CRPS values the River Oder is improved more by post-processing. This suggests that post-processing is more effective at dealing with certain types of error and therefore that the benefit of post-processing is catchment dependent. This is discussed in Sect. 5.2.

855   As mentioned, many of the stations with CRPSS values below 0 at short lead-times are degraded due to peak flows being better predicted by the raw forecasts. Therefore, the skill of the forecast at different flow levels is evaluated. Figure 10 shows the distribution of CRPSS values for all stations evaluated over the 4 quartiles of discharge (Q1 lower quartile to Q4 upper quartile) such that each boxenplot contains 522 CRPSS values, one for each station evaluated over approximately 52 forecasts. Only lead-times of 3, 6, 10, and 15 days are shown but these lead-times are representative of the results at similar lead-times.
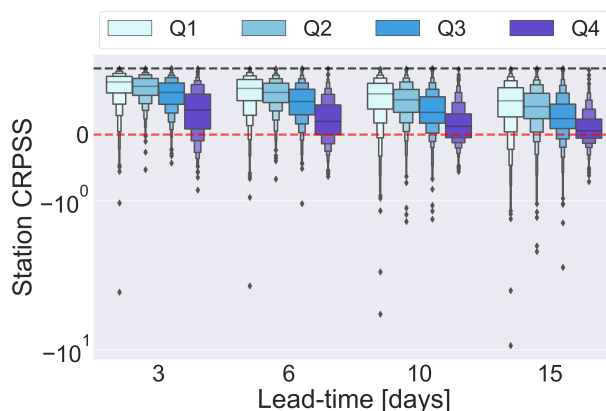
Figure 10. The Continuous Ranked Probability Skill Score (CRPSS) for all 522 stations calculated over the forecasts (approximately 52 forecasts) with flow values in the lowest quartile (Q1) to the highest quartile (Q4). CRPSS values below 0 indicate the forecast probability distribution is on average less skillful after post-processing and values above 0 indicate added skill after post-processing. A log-scale is used on the y-axis.

860   The improvement for all 4 quartiles decrease with lead-time as has been seen previously in Fig. 5 and Fig. 9. The improvement from post-processing is smaller for higher flows. However, the majority of stations are still improved for these high flows with over 60% of stations being improved for discharge values in Q4 at a lead-time of 15 days. The high flows are often under-predicted by both sets of forecasts. As discussed in Sect. 5.1.1, the ability of the post-processed forecasts to capture the magnitude of peaks is often determined by the relative spread of the hydrological and meteorological uncertainty distributions.

865   Although Q4 is the category with the greatest number of degraded stations (CRPSS < 0), some stations are degraded more (have a lower CRPSS value) for discharge values in Q1. This is mainly due to the larger proportional errors for lower flows.

5.2   What impacts the performance of the post-processing method?

In the previous section the impact of post-processing was shown to vary greatly between stations. The following sections investigate the factors that influence the effect of the post-processing method. The CRPSS is used in this analysis as it provides

870   an assessment of the improvement or degradation to the overall skill of the probabilistic forecast.

To aid the discussion of the key results some stations are highlighted. See Fig. 3 for the locations of the stations. Figure 11 shows the observed time-series (solid black line) for half the evaluation period (1 October 2017 to 30 September 2018) for six example stations; (a) Daldowie, Scotland. (b) Nytorp, Sweden. (c) Svarttjørnbekken, Norway. (d) Daugavpils, Latvia. (e) Porttipahta, Finland. (f) Montañana, Spain. The forecast median of the raw forecasts (oranges) and the post-processed

875   forecasts (purples) are also plotted for lead-times of 3 days (circles), 6 days (crosses), and 15 days (triangles). These stations are discussed throughout Sect. 5.2 and were chosen as they allow some of the impacts of the post-processing to be visualised. Table 2 summaries the key results that each of the example stations highlight and all results are summarised in Sect. 6.

5.2.1   Type of uncertainty

This section looks at how meteorological and hydrological uncertainties affect the performance of the post-processing method.

880   As mentioned in Sect. 1, the term meteorological uncertainties is used to refer to the uncertainty in the streamflow forecasts due to the error and uncertainty in the meteorological forcings, and not the error in the meteorological forecasts themselves. The magnitude of meteorological uncertainty is represented here by the CRPS of the raw ensemble forecast at each lead-time respectively. To remove the uncertainty due to the hydrological model, the water balance simulation is used as the "truth" value in the calculation of the CRPS, replacing the value of the observation, y, in Eq. (33). As both the forecast and the water balance

885   simulation are produced using the same hydrological model, and the water balance simulation provides the initial conditions for the reforecasts, the only remaining uncertainty is from the forcings. The errors of the meteorological observations used to create the water balance simulation are considered negligible compared to those of the meteorological forecasts. The magnitude of the hydrological uncertainty is represented by the CRPS of the water balance simulation, with the observations used as the "truth" values, at each lead-time respectively. As both these values are deterministic the CRPS is equivalent to the ~~square of the~~

890   ~~absolute difference~~ absolute error between the two values. Both metrics, for the meteorological and hydrological uncertainties, are averaged over all 208 forecasts for each station. So that the errors are comparable between catchments they are calculated in terms of specific discharge (~~$mm\,d^{-1}$~~ $mm\,d^{-1}$) instead of discharge ($m^3 s^{-1}$).
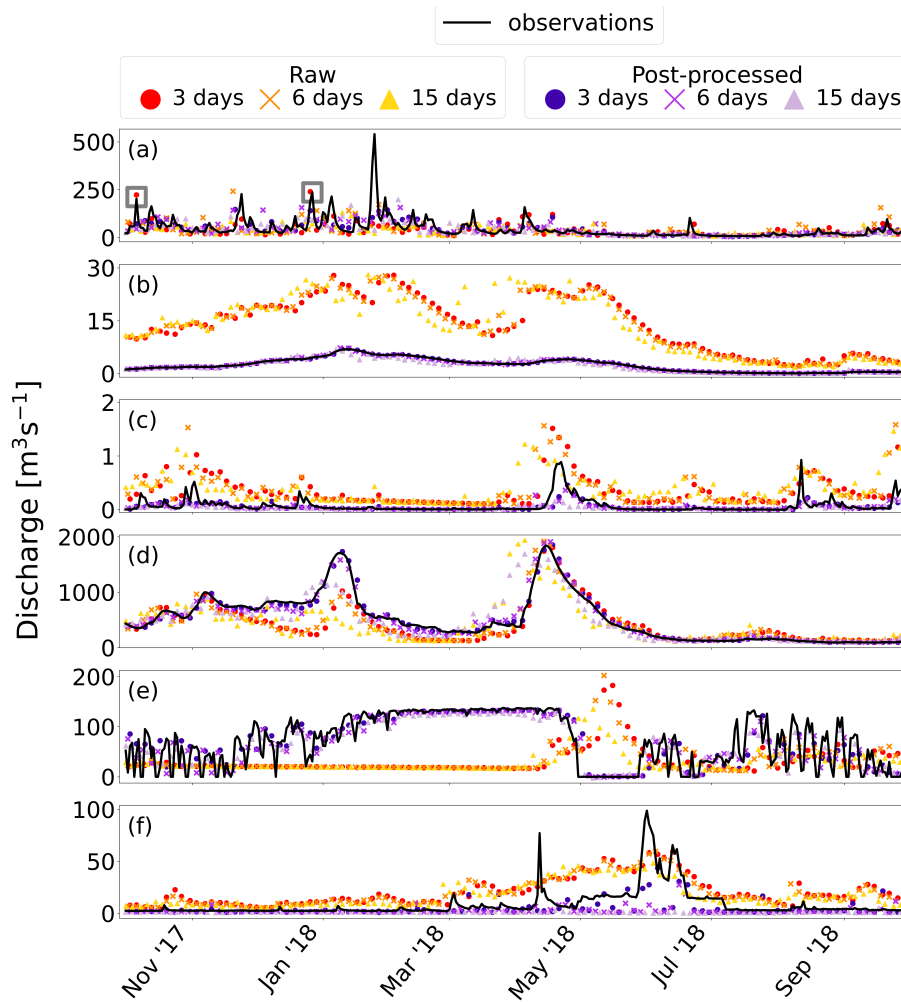
Figure 11. Observation time-series for one year of the evaluation period from October 2017 to October 2018 for 6 example stations. The forecast medians of the raw and post-processed forecasts are shown for lead-times of 3, 6, and 15 days. (a) Daldowie, Scotland. (b) Nytorp, Sweden. (c) Svarttjørnbekken, Norway. (d) Daugavpils, Latvia. (e) Porttipahta, Finland. (f) Montañana, Spain.

Figure 12 shows density plots of the CRPSS values for all stations vs the hydrological errors (a-c) and meteorological errors (d-f) for lead-times of 6, 10, and 15 days. A lead-time of 3 days is not shown here as the meteorological forcings have often

895 not had a significant effect on the forecasts resulting in a small distribution of meteorological errors across stations. However, the relationships discussed below are present at all lead-times. The 15 stations with the largest hydrological errors at each lead-time have been removed from the main analysis because these stations ~~appear to show a slightly~~ show a different pattern as shown in Fig. 12g and discussed below.

The purple lines in Fig. 12 show the least-squares regression line of best fit for the relationship between the CRPSS vs

900 the hydrological and meteorological errors. In general, an increase in either the hydrological or meteorological uncertainties,

Panel	Station	Description of key results	Section
(a)	Daldowie, Scotland	– Meteorological errors are not corrected as well as hydrological errors. – Poor post-processing of peaks for flashy catchments.	5.2.1, 5.2.2
(b)	Nytorp, Sweden	– Large biases due to limitations of the drainage network are well corrected.	5.2.1, 5.2.2
(c)	Svarttjørnbekken, Norway	– Post-processing is beneficial for stations where the hydrological model is uncalibrated.	5.2.2
(d)	Daugavpils, Latvia	– Slowly responding catchments benefit from post-processing the most. – Post-processing can account for poor modelling of slow hydrological processes such as snowmelt.	5.2.2
(e)	Porttipahta, Finland	– Regulated catchments benefit from post-processing.	5.2.2
(f)	Montañana, Spain	– The quality of the calibration time-series is more important than the length of the time-series.	5.2.3

Table 2. Key results and the section that provide more information for each of the six stations used as examples and for which time-series are shown in Fig. 11

decreases the improvement due to post-processing. However, this relationship is much stronger for the meteorological errors ~~, which account for over 13% of the variability observed in the CRPSS values whereas the hydrological errors only account for around 1% of this variability. This~~ $(r > 0.13$ compared to $r \approx 0.01$ for hydrological errors) which suggests that hydrological errors are better corrected by the post-processing method ~~and hence their magnitude has little impact on the performance of the~~

905 ~~post-processing method~~. The EMOS method is used to correct the spread of the raw forecast to account for the meteorological uncertainty (see Sect. 3.4.2) ~~. However, the EMOS method is not used to correct for any bias introduced by the meteorological forcings~~ but no bias correction is performed as is sometimes done ~~(e.g. Gneiting et al., 2005; Hemri et al., 2015b; Zhong et al., 2020) .Both~~ (e.g. Skøien et al. (2021); Gneiting et al. (2005); Hemri et al. (2015b); Zhong et al. (2020)). Whereas both bias and spread correction are performed for the hydrological uncertainties. In Sect. 5.1.4 it was noted that the raw forecasts for the Rhine and

910 the Oder catchments have similar skill but the Oder was improved more by post-processing. It was found (not shown) that
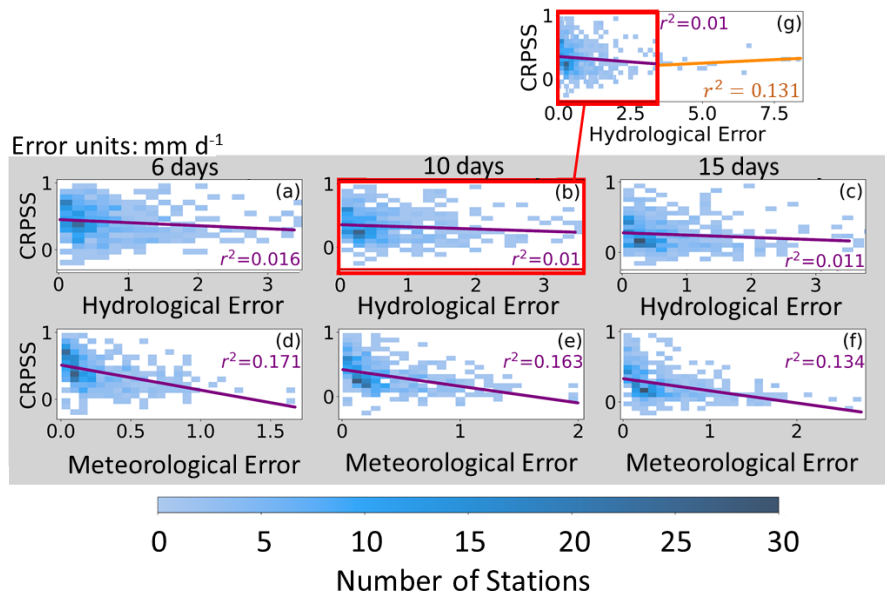
Figure 12. Density plots showing the station CRPSS for lead-times of 6 days (a and d), 10 days (b and e), and 15 days (c and f), against hydrological error (a-c) and meteorological error (d-f). The largest 15 hydrological errors are excluded from panels a-f. See Sect. 5.2.1 for an explanation of the metrics used to represent the hydrological and meteorological errors. Purple lines show the line-of-best-fit calculated using linear regression and the associated r^2 are given within each panel. (g) The CRPSS against hydrological error including the 15 largest hydrological errors for a lead-time of 10 days. The orange line shows the line-of-best-fit for the station with large hydrological errors.

this is because the errors in the raw forecast of the Rhine were mainly meteorological but those of the Oder were mainly hydrological.

Although the r^2 values are small some trends are observed in their variation with lead-time. The relationship between the meteorological errors and the CRPSS value is slightly stronger at shorter lead-times. This is partly because the EMOS spread correction parameters are lead-time invariant. The spread of the raw forecast tends to be ~~very~~ small at short lead-times, because all ensemble members have the same initial conditions, but increases as the differing meteorological forcings propagate through the catchment system. ~~Multiplying the spread at~~ Skøien et al. (2021) found that the value of the variance inflation factor (ζ in Eq. (20) of this paper) decreases with increasing lead-time even becoming less than 1 (a reduction in spread) for lead-times greater than 8 days (see top left panel of Fig. 8. in Skøien et al. (2021)). This alters the structure of the forecast spread increasing the uncertainty at shorter lead-times and decreasing the uncertainty at longer lead-times. However, here the spread at all lead-times is multiplied by a constant value ~~means~~ such that the spread retains ~~this~~ its original structure. Therefore, at shorter lead-times the meteorological forcings are more influential within the Kalman filter than at longer lead-times ~~(as discussed in Sect. 5.1.1).~~ On the one hand, if the raw forecast is skilled at short lead-times then this greater influence is beneficial and may, for example, allow the post-processed forecast to predict an upcoming peak. On the other hand, any large errors contained in the raw forecasts propagate through to the post-processed forecasts. ~~Meteorological errors are due~~

to the inaccuracy or the lack of confidence of the raw forecast and can impact the post-processed forecast as discussed in Sect. 5.1.1. For example, the largest peak in the time-series for the station in Daldowie, Scotland (see Fig. 11a) is not predicted by the raw forecast ~~medians and it is therefore~~ not predicted by the post-processed forecast ~~medians either because~~; therefore, no information about the ~~precipitation-driven upcoming~~ peak has been provided by the raw forecast. ~~As discussed in~~

930 ~~Sect. 5.1.1, the spread of the meteorological uncertainty distribution (see Sect. 3.4.2) relative to the spread of the~~ upcoming, precipitation-driven peak is provided to the post-processed forecast. Using a lead-time dependent EMOS method may allow for better use of the information provided by meteorological forcings.

Alternatively, the hydrological uncertainty distribution ~~(see Sect. 3.4.1) determines the weight of each~~ may have a greater weight within the Kalman filter ~~and hence their impact on the post-processed forecast. Figure 11a shows that many of the~~. Some

935 peaks at the Daldowie station in winter 2017/2018 are forecast accurately by the raw forecast median (grey boxes in Fig. 11a) but are not forecast by the post-processed forecast. This suggests that the hydrological uncertainty distribution is most impactful in the Kalman filter. The observations in the recent period often don't indicate an upcoming flood ~~so the conditioning on these observations results~~ resulting in a hydrological uncertainty distribution which confidently, but incorrectly, predicts a low flow. The confidence of the hydrological uncertainty distribution ~~has a larger weighting in the Kalman filter due to its confidence~~

940 ~~which~~ results in the information of the upcoming flow provided by the meteorological uncertainty distribution being ignored. This ignoring of the meteorological information is also the reason for the poorly post-processed forecasts for some stations in Spain (see Fig. 9) ~~. As some Mediterranean catchments~~ which have very low hydrological variability except for rare large peaks ~~, it is unlikely that observations from the recent period will indicate an upcoming peak, and therefore, the hydrological uncertainty distribution usually predicts a low flow with very high confidence. As this will often lead to the meteorological~~

945 ~~forcings being ignored, even though~~. Since extreme precipitation can be an important runoff generating mechanism in this region (Berghuijs et al., 2019), post-processed forecasts for these catchments should be used cautiously particularly when the raw forecasts predict a flood.

For the hydrological errors the r^2 values decrease for lead-times of ~~10 and 15 days are similar whereas the r^2 value for a lead-time of 6 days is slightly higher. In general, the r^2 value decreases for lead-times of~~ 1 day to approximately 6 days (not

950 shown) and for lead-times longer than 6 days the r^2 values remain at approximately 0.01. This suggests that forecast dependent errors due to the initial conditions and the interaction of the meteorological forcings in the hydrological model are corrected at shorter lead-times, but at longer lead-times the correction is mainly to consistent hydrological model errors. ~~The consistent hydrological errors can be corrected well regardless of magnitude.~~

The 15 stations with the largest hydrological uncertainties ~~is~~ show a small increase in average CRPSS with increasing

955 hydrological uncertainties. This trend is visualised by the orange line in Fig. 12g but the limited number of data points makes the calculation irresolute. The relationship is only shown here for a lead-time of 10 days but is present at all longer lead-times. Most of the hydrological uncertainty in these cases is caused by large consistent biases rather than forecast dependent errors. ~~These consistent biases are usually easier to correct resulting in higher CRPSS values when the bias of the raw forecasts is larger.~~ For example, ~~one of the 15 stations with the largest hydrological uncertainties is the~~ the station in Nytorp, Sweden

960 ~~which~~ has a large bias in the raw forecasts (see Fig. 11b). As discussed in 5.1.1 the post-processing method is able to correct

for consistent biases ~~by conditioning the climatological forecast on the discharge values in the recent period. This results in resulting in~~ post-processed forecasts that much more closely follow the observations as shown in Fig. 11b ~~, and large KGESS and CRPSS values at all lead-times~~ and higher CRPSS values when the bias of the raw forecasts is larger.

5.2.2 Catchment characteristics

The catchments within the EFAS domain vary greatly in terms of size, location, and flow regime. This section discusses catchment characteristics that impact the performance of the post-processing method namely: upstream area, response time, elevation, and regulation. In Fig. 13, box-and-whisker plots are used to show the distribution of the CRPSS values for all stations at every other timestep with the whiskers extending to the 5th and 95th percentiles. The stations are split into categories depending on (a) the size of the upstream area, (b) the time of concentration, and (c) the elevation. Values for these characteristics are extracted from static LISFLOOD maps used operationally.

Figure 13a shows that in general large catchments (larger than 5000 km^2) are improved more by post-processing than medium (between 1000 km^2 and 5000 km^2) and small (less than 1000 km^2) catchments. ~~The difference is largest at shorter~~, particularly at short lead-times ~~and decreases until near negligible at a lead-time of 15 days~~. The relationship between medium and small catchments is less consistent. At short lead-times the median CRPSS value for small catchments is higher than for medium catchments but for longer lead-times the converse is true. However, it was found that by removing stations with an upstream area smaller than 500 km^2 (henceforth referred to as very small catchments) from the analysis the remaining small stations (with upstream areas between 500 km^2 and 1000 km^2) are in general improved less by post-processing than medium catchments at all lead-times. This results in a single trend: that in general post-processing improves forecasts more for larger catchments. ~~The need to remove~~ A partial reason for this is that smaller catchments are impacted more by spatiotemporal errors in the meteorological forcings than larger catchments (Pappenberger et al., 2011) and, as discussed in Sect. 5.2.1, meteorological errors are difficult to correct.

There are two reasons why very small catchments ~~from the analysis~~ must be removed to clearly identify ~~this trend is due to 1) uncalibrated stations and 2) errors in the upstream areas. Both reasons complicate the relationship~~ the trend between upstream area and CRPSS ~~values for very small catchments and are discussed below.~~

~~Most~~. Firstly, most stations with upstream areas (provided by local authorities) smaller that 500 km^2 were not included in the calibration of LISFLOOD for EFAS 4 (Mazzetti et al., 2021b). ~~Whilst for~~ The uncalibrated model has varying skill between catchments with some very small catchments ~~the uncalibrated model may have good hydrological skill, for others the exclusion from calibration may result in larger hydrological errorsthan for calibrated catchments~~ having large hydrological errors. As discussed in Sect. 5.2.1 hydrological errors are well-corrected by post-processing, therefore resulting in larger CRPSS values for some very small uncalibrated catchments than for larger calibrated catchments ~~where the errors may be primarily meteorological. For example, the station in Svarttjørnbekken, Norway has a catchment area provided by local authorities of 3.4 km^2 and was therefore not included in the calibration. Fig. 11c shows that the raw forecasts over-estimate the variability of the flow resulting in large over-estimations of the magnitude of the peaks. This is likely due to the lack of model calibration at this station.~~
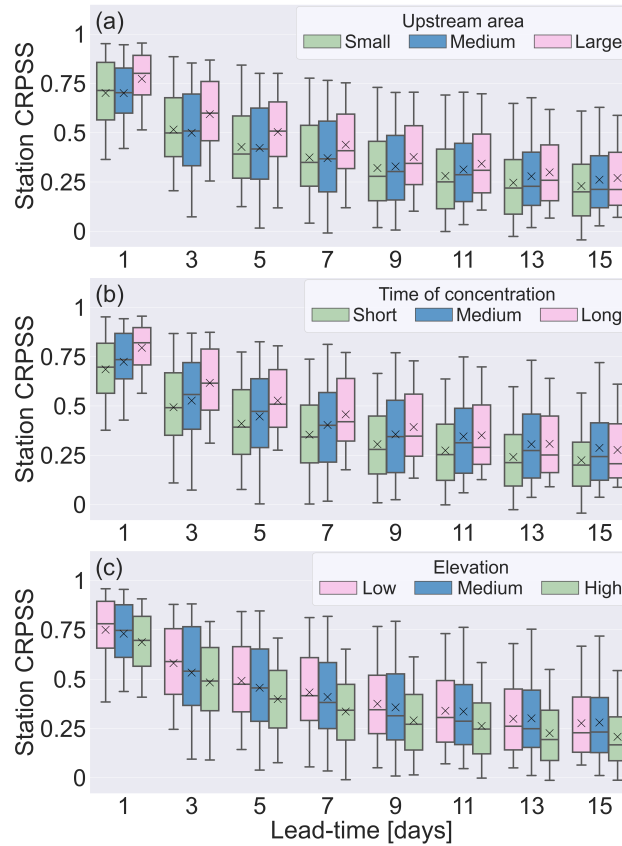
Figure 13. The CRPSS for all 522 stations at every other lead-time with stations categorised by their catchment characteristics. (a) Upstream area. Small catchments: less than 1000 km^2 (165 stations), Medium catchments: between 1000 km^2 and 5000 km^2 (204 stations), Large catchments: larger than 5000 km^2 (153 stations). (b) Time of concentration. Fast response catchments: less than 24 hours (253 stations), Medium response catchments: between 24 and 48 hours (144 stations), Slow response catchments: more than 48 hours (126 stations). (c) Elevation Low-elevation catchments: less than 150 ~~m~~ m (178 stations), Medium-elevation catchments: between 150 ~~m~~ m and 400 ~~m~~ m (168 stations), High-elevation catchments: more than 400 ~~m~~ m (177 stations)

995 ~~The~~. Secondly, the minimum area increment of the LISFLOOD static map used to categories the stations is the area of one grid-box, 25 km^2. Therefore, the upstream areas are multiples of 25 km^2 and thus may not ~~match those provided by local authorities. The~~ represent the real size of the catchment which could lead to large hydrological biases. For example, the station in Svarttjørnbekken~~Norway is also impacted by this over-estimation of the upstream area. In~~, Norway has a catchment area provided by local authorities of 3.4 km^2 and was therefore not included in the calibration. Additionally, in LISFLOOD its

1000 upstream area ~~of 3.4 km²~~ is rounded to 25 km^2 (over 7 times the size of the catchment). ~~As shown in Fig. 11c , this~~ Figure 11c shows that these issues result in an over-estimation of the ~~upstream area results in~~ variability of the flow and a consistent bias in the raw forecast even at low flows. ~~The post-processed forecasts are bias corrected as discussed in Sect. 5.1.1. Errors in~~

~~the upstream area occur for stations of all sizes but in general are proportionally larger for very small catchments.~~ Both issues are corrected by post-processing.

1005   In Fig. 13b the time of concentration is used to represent the catchment response time. Stations are split into fast response catchments (response times of less than less than 24 hours), moderate response catchments (between 24 and 48 hours), and slow response catchments (more than 48 hours). At short lead-times, slowly responding catchments outperform medium and fast responding catchments. Since large catchments tend to have slower responses, this suggests response time is partly responsible for the greater improvement experienced by large catchments. Slower responses result in stronger autocorrelations therefore

1010 the ~~relationship between discharge values in the recent period and those in the forecast period are stronger. Therefore allowing greater improvements for slowly responding catchments than for flashier catchments.~~ recent observation are more informative about the state of the river during the forecast period. This is shown by comparing the time-series of the Daugavpils station (Fig. 11d) which has a time of concentration of approximately 195 hours with that of the Daldowie station (Fig. 11a) which has a time of concentration of 27 hours. The Daugavpils station has a slow response with peaks lasting two months (longer than the length

1015 of the recent period) whereas the Daldowie station responds faster with peaks only lasting a week at most (shorter than the length of the forecast period). As such the post-processing method can correct forecasts much better for the Daugavpils station. ~~Additionally, as mentioned in Sect. 2, the forecasts have daily timesteps and the forecast variable is the average discharge over the preceding 24 hours. For fast response catchments this means that the entire duration of the catchment response may be contained within a single timestep which can makes peak-time errors more damaging to the forecast. In Sect. 5.1.2 the~~

1020 ~~post-processed forecasts were found to have larger timing errors than the raw forecasts. This is likely to have contributed to the worse performance of the post-processing method for fast response catchments compared to slow response catchments.~~

    ~~Figure 13b shows at longer lead-times the improvements to medium and slowly responding catchments are similar but the fast response catchments remain least improved. However,~~ It should be noted that most stations still benefit from being post-processed even at lead-times larger than their time of concentration. This is useful as operationally there is a delay in the

1025 availability of ~~observations (both discharge observations and~~ the meteorological observations used to create the water balance simulation ~~)~~ whereas here it is assumed that all observations up to the production time of the reforecast are available. Therefore, these results suggest that although the CRPSS may be smaller there is still an operational benefit to post-processing.

    In Fig. 13c catchments are categorised by the height of the station above sea level: low-elevation catchments (less than 150 m), medium-elevation catchments (between 150 m and 400 m), and high-elevation catchments (more than 400 m). At all

1030 lead-times catchments at higher elevations are improved less than lower-lying catchments. This is partly due to mountainous catchments tending to have faster response times. Additionally, ~~as shown in Sect. 5.2.1, the post-processing is sensitive to meteorological errors. Precipitation~~ precipitation forecasts in mountainous regions can be biased due to insufficient resolutions to represent the orography in the NWP systems ~~(Lavers et al., 2021; Haiden et al., 2014)~~ (Lavers et al. (2021); Haiden et al. (2014); Haiden et al. (2021b)). Alfieri et al. (2014) found that when compared to the water balance simulation (i.e. equivalent to the

1035 metric for meteorological error used here) the raw ensemble forecasts are negatively biased in mountainous regions due to an under-estimation of the precipitation. ~~In addition to under-estimation of the precipitation amount, spatial and temporal errors in the meteorological forecast can lead to errors in the streamflow forecasts. Spatio-temporal errors are more damaging for small~~
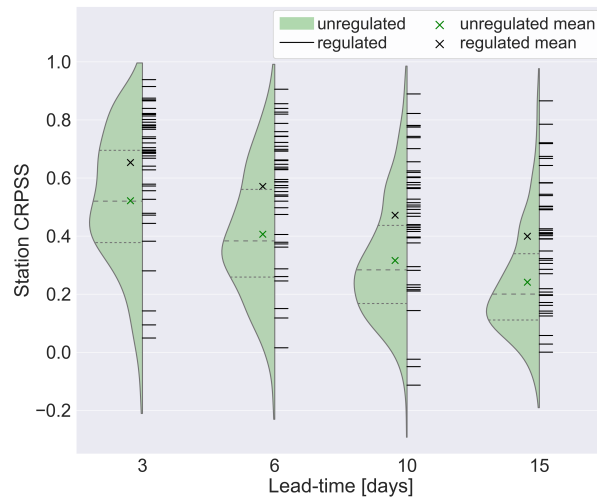
Figure 14. Violin plot of the CPRSS values for the 480 unregulated stations (green distribution) and the 42 regulated catchments (black lines) at lead-times of 3, 6, 10, and 15 days.

~~catchments (Pappenberger et al., 2011) and tend to increase with lead-time (Haiden et al., 2014, 2021b). Since catchment area tends to decrease at higher elevations this could account for the slight increase in the difference in CRPSS values between~~
1040   ~~high-elevation catchments and lower-lying catchments at longer lead-times.~~ The effect of station elevation on the performance of the post-processing method explains the cluster of degraded stations around the Kjolen Mountains (see Fig. 9).

    The regulation of rivers via reservoirs and lakes is difficult to model. Raw forecasts for many regulated catchments were found to have negative correlation with the observations ~~(not shown) including the Porttipahta station in Finland which had the worst raw correlation of all stations. The improvement due to post-processing at regulated stations is dependent on whether~~
1045   ~~the reservoir is in the same state during the recent and forecast periods and hence whether the discharge values from the recent period provide useful information about the state of the reservoir.~~. In this study, a station is considered regulated if it is within 3 grid-boxes downstream of a reservoir or lake in the LISFLOOD domain or if data providers have reported that the station is on a regulated stretch of the river. Figure 14 shows the CRPSS values of the 42 regulated stations (black lines) and the distribution of the CRPSS values of the unregulated stations (green distribution) for lead-times of 3, 6, 10, and 15 days. The distribution
1050   for the unregulated stations is estimated using kernel density estimation with the dashed line showing the median value and the dotted lines showing the interquartile range. The mean CRPSS values are indicated by crosses of the respective colours.

    At all lead-times, the CRPSS values of most regulated stations are above the median of the unregulated stations. Additionally, the mean CRPSS value of the regulated stations is at least 0.1 higher than that of the unregulated stations for all lead-times longer than 1 day. ~~At short lead-times the difference is smaller because the recent discharge values are similarly informative~~
1055   ~~for both sets of stations. The largest difference in mean CRPSS values is at a lead-time of 6 days. By this lead-time the recent discharge values are less relevant for unregulated catchments. However, if the~~ The improvement due to post-processing at regulated stations is dependent on whether the reservoir is in the same state ~~as~~ during the recent ~~period, then the recent~~

~~observations remain relevant for regulated catchments allowing for greater improvement~~and forecast periods and hence whether the discharge values from the recent period provide useful information about the state of the reservoir. At longer lead-times it becomes more likely that the reservoir will have changed state and therefore that the information provided by the recent discharge values is not useful. However, if the reservoir is in the same state then the magnitude of the improvement from post-processing can be large. For example, the Porttipahta station in Finland is located at the Porttipahta reservoir and its time-series is shown in Fig. 11e. In May 2018 the discharge is 0 ~~$m^3 s^{-1}$~~ $m^3 s^{-1}$ for approximately a month. The raw forecast does not capture this decrease in discharge, but the post-processed forecast median is very accurate even at longer lead-times. However, at the start and end of this zero-flow period the post-processed forecasts do not perform as well for a lead-time of 15 days (purple triangles) ~~. This is~~ because the reservoir has changed state since the forecast production time~~and therefore the recent observations are not providing correct information about the state of the reservoir. The Porttipahta has a correlation component of the KGE' of approximately -0.5 at all lead times for the raw forecast but post-processing increases this to between 0.91 and 0.68 at all lead-times.~~

~~If the reservoir changes state often the skill of the post-processed forecasts is less consistent. Small but regular controlling of the flow via reservoirs can create poorly performing post-processed forecasts. For example, the post-processed forecasts are not able to capture the relatively rapid oscillation in the autumn and winter months of the Porttipahta time-series as well as they do the month long zero-flow period in the summer (see Fig. 11e).~~ It is thought that small but regular regulation is partly responsible for the cluster of degraded stations on the River Sava shown for a lead-time of 10 days in Fig. 9c. Three of the degraded stations in this cluster are regulated and are the three regulated stations with the lowest CRPSS values at all lead-times shown in Fig. 14.

It is interesting to consider whether other hydrological processes that are difficult to model can be accounted for by post-processing. For example, the peak in the winter and spring in the Daugavpils catchment (see Fig. 11d) is largely dominated by snow and ice melt (Škute et al., 2008) ~~. Snowmelt is known to be a difficult process~~ which are difficult processes to model (Alfieri et al., 2014). ~~As shown in Fig. 11d~~ Figure 11d shows that the raw forecasts do not predict the ~~large~~ magnitude of the peak in late January but the post-processed forecasts~~are able to capture the peak due to their conditioning~~, which are conditioned on recent observations ~~which include~~ that indicate the increase in discharge due to snowmelt, do accurately predict the peak. Similar results were seen in other catchments with snow dominated regimes. Although the identification of dominating runoff generating mechanisms for all catchments and seasons is beyond the scope of this study, the results presented in this section suggest that post-processing can correct for errors introduced by the imperfect modelling of slow hydrological processes.

5.2.3 Calibration time-series

The length of the ~~historic period, and therefore the length of the~~ time-series used to calibrate the station model ~~,~~ varies between stations. The maximum length is dictated by the ~~corresponding~~ water balance simulation which is available from 1 January 1990. However, many stations have shorter time-series due to the availability of observations. ~~The lengths of the calibration time-series of the evaluated stations vary from 2 to 27 years with a mean of 21 years and a median of 23 years. This distribution is heavily skewed towards longer time-series compared to the distribution for all operationally post-processed~~

~~stations. Operationally only 45% of stations have time-series greater than 20 years and 25% have time-series of less than 5 years whereas within the evaluated stations 70% have time-series over 20 years and only 5% have time-series less than 5 years. The difference in the distribution of time-series lengths is due to the criteria used to select the stations for evaluation. Many of~~
1095 ~~the stations with short time-series have an overlap between the evaluation and calibration periods and therefore cannot be used.~~

Figure 15 shows the CRPSS values for each lead-time with stations split by the length of their calibration time-series into unequally sized categories (see caption): very short time-series (up to 15 years), short time-series (between 15 and 20 years), medium time-series (between 20 and 25 years), and long time-series (over 25 years). These categories were chosen to
1100 investigate the impact of the length of the calibration time-series whilst keeping the number of stations in each category as large as possible. These initial comments ignore the very short time-series (green) which are discussed in more detail below. ~~For~~

At short lead-times ~~up to 3 days,~~ long time-series in general lead to more improvement by post-processing than shorter time-series. ~~For lead-times from 3 to 7 days there is little difference between the performance of the post-processing at stations~~
1105 ~~with medium times-series (pink) and long time-series (yellow) but the performance is lower for stations with short time-series.~~ Longer time-series allow the joint distribution between the observations and the water balance simulation to be more rigorously defined allowing a more accurate conditioning of the forecast on the discharge values from the recent period. For lead-times greater ~~that~~ than 7 days the CRPSS distributions for all categories are similar. As discussed in Sect. 5.2.1, post-processing corrects forecast specific errors at short lead-times but at longer lead-times it is mainly consistent errors to the climatology
1110 that are corrected. The similarity of the CRPSS distributions suggests that short time-series are sufficient to capture these consistent errors. ~~As the calibration time-series of the evaluated stations tend to be longer than that of the average operationally post-processed station~~This is also shown by the relatively good performance of stations with very short time-series. Although a full sensitivity analysis is beyond the scope of this study, these results suggest that ~~the average improvement at short lead-times may be over-estimated~~very short time-series can be used, if necessary, to correct for consistent biases, although
1115 longer time-series are preferable. However, ~~as the evaluated stations are also operationally post-processed these results are still indicative of the improvement expected operationally at some stations.~~ care should be taken when forecasting high flows since a short timeseries will not allow for a robust calculation of the upper tail of the discharge distribution (see Sect. 3.3.1) which will likely cause errors in the forecast probability distribution (Bogner et al., 2012).

~~At the longest lead-times there is a small decrease in the CRPSS for longer~~ In general, shorter time-series ~~. This slight trend~~
1120 ~~may be due to the different sizes of the categories, but it may also suggest that longer time-series are more likely to include non-stationary patterns. There are several reasons that this can occur at a station. A non-exhaustive list includes changes to the rating curve due to river channel alterations, changes to the joint distribution due to catchment modifications, and errors in the observations due to instrument failure~~tend to be more recent and so benefit from improved river gauging technology and also because non-stationarity between the calibration and evaluation period is less likely to be an issue. The station in
1125 Montañana (shown in Fig. 11f) is an example of a station where a period of poor quality observations in the calibration time-series impact the calibration resulting in a large jump in the CDF of the observed discharge distribution as highlighted by a red
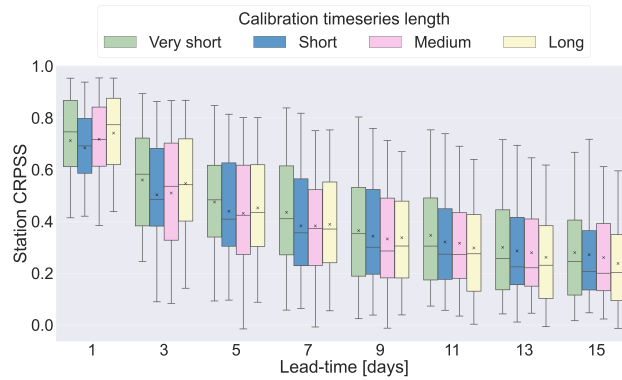
Figure 15. The CRPSS for all 522 stations at every other lead-time with stations categorised by the length of their calibration time-series. Very short time-series: less than 15 years (63 stations), Short time-series: 15 to 20 years (93 stations), Medium time-series: 20 to 25 years (119 stations), Long time-series: over 25 years (247).
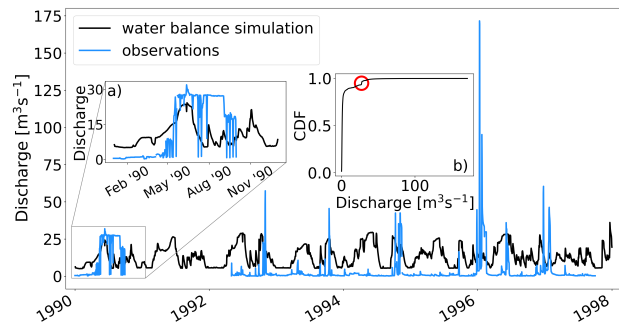
Figure 16. Observations (blue) and water-balance simulation (black) time-series used in the calibration of the station model for the station in Montañana. a) Section of the calibration time-series with errors in the observations. b) the Cumulative Distribution Function (CDF) of the observed discharge distribution calculated during the calibration. Red circle indicates a jump in the CDF due to the section of the time-series shown in a).

circle in Fig. 16b. This CDF is used in the NQT and the large jump results in non-smooth forecast probability distributions. Additionally, these errors were found to impact the estimation of the joint distribution . The Montañana station has the lowest correlation value which resulted in a decrease in the correlation coefficient after post-processing(see Fig. 5) due to a degradation

1130   in the correlation of approximately 0.7. This may be due to the poorly defined joint distribution. This example highlights the importance of the quality of the observation data especially in short time-series where each observation has more impact on the estimated distributions. Even stations with time-series of less than 5 years are corrected for both consistent biases and forecast dependent errors by post-processing. This suggests . Removing the erroneous observations improved the discharge estimations suggestsing that the priority should be to use the best quality data available even if that means that the the resultant calibration

1135   time-series is shortshorter.

6 Conclusions

Post-processing is a computationally efficient method of quantifying uncertainty and correcting errors in streamflow forecasts. Uncertainties enter the system from multiple sources including the meteorological forcings from numerical weather prediction systems (here referred to as meteorological uncertainties), and the initial hydrological conditions and hydrological model (here referred to as hydrological uncertainties). The post-processing method used operationally in the European Flood Awareness System (EFAS) uses a method motivated by the Ensemble Model Output Statistics (Gneiting et al., 2005) method to account for the meteorological uncertainty and the Multi-Temporal Model Conditional Processor (Coccia, 2011) to account for the hydrological uncertainty. The EFAS domain includes catchments of varying characteristics for which the same post-processing method is used. In this paper we used reforecasts to investigate the added skill gained by post-processing and how these improvements vary across the domain. This study aimed to answer two research questions.

First, does the post-processing method provide improved forecasts? Our results show that for the majority of stations the post-processing improves the skill of the forecast with median Continuous Ranked Probability Skill Scores (CRPSS) of between 0.74 and 0.2 at all lead-times. This improvement is greatest at shorter lead-times of up to 5 days but post-processing is still beneficial up to the maximum lead-time of 15 days. The bias and spread correction provided by the post-processing increases the reliability of the forecasts and increased the number of correctly forecast flood events without increasing the number of false alarms. However, the post-processed forecasts also led to the flood peak often being forecast too early by approximately a day. Although, forecasts for floods events at most stations did benefit from post-processing the greatest improvements were to forecasts for normal flow conditions.

Second, what affects the performance of the post-processing method? Several factors were found to impact the performance of the post-processing method at a station. The post-processing method is more easily able to correct hydrological errors than meteorological errors. This is mainly because no bias-correction is performed for the meteorological errors whereas hydrological errors are bias corrected by conditioning the forecast on the recent observations. Therefore, stations where the errors were primarily due to hydrological errors were improved more. As the hydrological errors tend to be larger than the meteorological errors this is beneficial; however, more research is required to fully account for biases due to the meteorological forcings as well.

The post-processing method was found to easily account for consistent hydrological biases that were often due to limitations in the model representation of the drainage network. However, the correction of forecast specific errors (due to initial conditions

and meteorological forcings) was largely determined by the response time of the catchment. Therefore, the greatest improvement was seen in catchments larger than 5000 km^2 and catchments less than 100 m above sea level as these catchments tended to have longer response times. Additionally, post-processing was able to correct for errors due to difficult to model hydrological processes, such as regulation and snowmelt, when recent observations contained relevant information about the discharge.

The use of long historic observational time-series for the offline calibration is beneficial particularly for correcting forecast specific errors. However, time-series shorter than 15 years were found to be sufficient for correcting consistent errors in the model climatology even at a lead-time of 15 days. The quality of the observations in the historic time-series is important and errors in the time-series degraded the performance of the post-processing method and limit the usefulness of the forecasts.

These results highlight the importance of post-processing within the forecasting chain of large-scale flood forecasting systems. They also provide a benchmark for end-users of the EFAS forecasts and show the situations when the post-processed forecasts can provide more accurate information that the raw forecasts. These results also highlight possible areas of improvement within the EFAS and the factors that must be considered when designing and implementing a post-processing method for large-scale forecasting systems.

Code and data availability. The raw reforecasts (https://doi.org/10.24381/cds.c83f560f) and the water balance simulation (https://doi.org/10.24381/cds.e3458969) are available from the Copernicus Climate Data Store. The post-processed forecasts and evaluation code are available from the University of Reading Research Data Archive (http://dx.doi.org/10.17864/1947.333).

Author contributions. GM: Conceptualization, data curation, formal analysis, investigation, methodology, project administration, software, validation, visualization, writing - original draft preparation, writing - review editing, CB: data curation, resources, software, HC: Conceptualization, Funding acquisition, methodology, project administration, supervision, writing – review editing, SD: Conceptualization, Funding acquisition, methodology, project administration, supervision, writing – review editing, TJ: Resources, software, CM: Resources, writing – review editing, CP: Conceptualization, Funding acquisition, methodology, project administration, supervision, writing – review editing.

Competing interests. The authors declare that they have no conflict of interest.

Acknowledgements. We gratefully acknowledge the financial support provided by the following: Gwyneth Matthews is funded in part by the EPSRC DTP 2018-19 University of Reading (EP/R513301/1) and ECMWF. Sarah Dance was funded in part by the UK EPSRC DARE project (EP/P002331/1) and the UK NERC National Centre for Earth Observation (NCEO). Hannah Cloke acknowledges funding from UK Natural Environmental Research Council (NERC): The Evolution of Global Flood Risk (EVOFLOOD) Project Grant NE/S015590/1. We thank Paul Smith for the development and operational implementation of the post-processing method. We are grateful for the advice provided by Shaun Harrigan and David Richardson. We thank members of the Water@Reading research group for their advice and support.

References

Abramowitz, M. and Stegun, I. A.: Handbook of mathematical functions with formulas, graphs, and mathematical tables, Dover Publications, Inc., New York, 1972.

Alfieri, L., Pappenberger, F., Wetterhall, F., Haiden, T., Richardson, D., and Salamon, P.: Evaluation of ensemble streamflow predictions in Europe, Journal of Hydrology, 517, 913–922, 2014.

Alizadeh, B., Limon, R. A., Seo, D.-J., Lee, H., and Brown, J.: Multiscale postprocessor for ensemble streamflow prediction for short to long ranges, Journal of Hydrometeorology, 21, 265–285, 2020.

Arnal, L., Asp, S., Baugh, C., De Roo, A., Disperati, J., Dottori, F., Garcia, R., GarciaPadilla, M., Gelati, E., Gomes, G., et al.: EFAS upgrade for the extended model domain–technical documentation, Tech. rep., JRC Technical Reports, EUR 29323 EN, Publications Office of the European . . . , 2019.

Arroyo, M. and Montoya-Manzano, G.: Real Time Quality Checks, https://efascom.smhi.se/confluence/display/EHDCC/5.2, accessed: 2021-04-30, 2019.

Baldauf, M. and Wetterdienst, D.: The COSMO model: towards cloud-resolving NWP, in: Recent Developments in Numerical Methods for Atmosphere and Ocean Modelling-Proceedings of a Seminar, pp. 107–122, 2014.

Barnard, C., Krzeminski, B., Mazzetti, C., Decremer, D., Carton de Wiart, C., Harrigan, S., Blick, M., Ferrario, I., F, W., and Prudhomme, C.: Reforecasts of river discharge and related data by the European Flood Awareness System version 4.0, https://doi.org/10.24381/cds.c83f560f, Accessed: 2021-03-04, 2020.

Berghuijs, W. R., Harrigan, S., Molnar, P., Slater, L. J., and Kirchner, J. W.: The relative importance of different flood-generating mechanisms across Europe, Water Resources Research, 55, 4582–4593, 2019.

Bogner, K. and Kalas, M.: Error-correction methods and evaluation of an ensemble based hydrological forecasting system for the Upper Danube catchment, Atmospheric Science Letters, 9, 95–102, 2008.

Bogner, K., Pappenberger, F., and Cloke, H.: The normal quantile transformation and its application in a flood forecasting system, Hydrology and Earth System Sciences, 16, 1085–1094, 2012.

Boucher, M.-A., Perreault, L., Anctil, F., and Favre, A.-C.: Exploratory analysis of statistical post-processing methods for hydrological ensemble forecasts, Hydrological Processes, 29, 1141–1155, 2015.

Brown, J., Ramos, M.-H., and Voisin, N.: Intercomparison of streamflow postprocessing techniques: first results of a HEPEX community experiment, in: EGU General Assembly Conference Abstracts, pp. EGU2013–8221, 2013.

Brown, J. D. and Seo, D.-J.: A nonparametric postprocessor for bias correction of hydrometeorological and hydrologic ensemble forecasts, Journal of Hydrometeorology, 11, 642–665, 2010.

Brown, J. D. and Seo, D.-J.: Evaluation of a nonparametric post-processor for bias correction and uncertainty estimation of hydrologic predictions, Hydrological Processes, 27, 83–105, 2013.

Cloke, H. and Pappenberger, F.: Ensemble flood forecasting: A review, Journal of hydrology, 375, 613–626, 2009.

Coccia, G.: Analysis and developments of uncertainty processors for real time flood forecasting, Ph.D. thesis, Alma Mater Studiorum University of Bologna, https://doi.org/10.6092/unibo/amsdottorato/3423, 2011.

Coccia, G. and Todini, E.: Recent developments in predictive uncertainty assessment based on the model conditional processor approach, Hydrology and Earth System Sciences, 15, 3253–3274, 2011.

COSMO: COSMO Limited-Area Ensemble Prediction System, http://www.cosmo-model.org/content/tasks/operational/leps/, last accessed: 2021-10-07, 2020.

1235 Crochemore, L., Ramos, M.-H., and Pappenberger, F.: Bias correcting precipitation forecasts to improve the skill of seasonal streamflow forecasts, Hydrology and Earth System Sciences, 20, 3601–3618, 2016.

Dance, S. L., Ballard, S. P., Bannister, R. N., Clark, P., Cloke, H. L., Darlington, T., Flack, D. L., Gray, S. L., Hawkness-Smith, L., Husnoo, N., et al.: Improvements in forecasting intense rainfall: Results from the FRANC (Forecasting Rainfall exploiting new data Assimilation techniques and Novel observations of Convection) project, Atmosphere, 10, 125, 2019.

1240 De Roo, A., Wesseling, C., and Van Deursen, W.: Physically based river basin modelling within a GIS: the LISFLOOD model, Hydrological Processes, 14, 1981–1992, 2000.

de Zea Bermudez, P. and Kotz, S.: Parameter estimation of the generalized Pareto distribution—Part I, Journal of Statistical Planning and Inference, 140, 1353–1373, 2010.

Deutscher Wetterdienst: Regional model COSMO-EU, https://www.dwd.de/EN/research/weatherforecasting/num_modelling/01_num_
1245 weather_prediction_modells/regional_model_cosmo_eu.html, last accessed: 2021-10-07, 2015a.

Deutscher Wetterdienst: ICON (Icosahedral Nonhydrostatic) Model, https://www.dwd.de/EN/research/weatherforecasting/num_modelling/01_num_we, last accessed: 2021-10-07, 2015b.

Dey, D. and Rao, C.: Handbook of Statistics, vol. 25, 2006.

EFAS: Meteorological forecasts, https://www.efas.eu/en/meteorological-forecasts, accessed: 2021-04-30, 2020.

1250 Ferro, C. A., Richardson, D. S., and Weigel, A. P.: On the effect of ensemble size on the discrete and continuous ranked probability scores, Meteorological Applications: A journal of forecasting, practical applications, training techniques and modelling, 15, 19–24, 2008.

Field, C. B., Barros, V., Stocker, T. F., and Dahe, Q.: Managing the risks of extreme events and disasters to advance climate change adaptation: special report of the intergovernmental panel on climate change, Cambridge University Press, 2012.

Flack, D. L., Skinner, C. J., Hawkness-Smith, L., O'Donnell, G., Thompson, R. J., Waller, J. A., Chen, A. S., Moloney, J., Largeron, C.,
1255 Xia, X., et al.: Recommendations for improving integration in national end-to-end flood forecasting systems: An overview of the FFIR (Flooding From Intense Rainfall) programme, Water, 11, 725, 2019.

Georgakakos, K. P., Seo, D.-J., Gupta, H., Schaake, J., and Butts, M. B.: Towards the characterization of streamflow simulation uncertainty through multimodel ensembles, Journal of hydrology, 298, 222–241, 2004.

Gneiting, T.: Making and evaluating point forecasts, Journal of the American Statistical Association, 106, 746–762, 2011.

1260 Gneiting, T.: Calibration of medium-range weather forecasts, European Centre for Medium-Range Weather Forecasts, 2014.

Gneiting, T., Raftery, A. E., Westveld III, A. H., and Goldman, T.: Calibrated probabilistic forecasting using ensemble model output statistics and minimum CRPS estimation, Monthly Weather Review, 133, 1098–1118, 2005.

Gupta, H. V., Kling, H., Yilmaz, K. K., and Martinez, G. F.: Decomposition of the mean squared error and NSE performance criteria: Implications for improving hydrological modelling, Journal of hydrology, 377, 80–91, 2009.

1265 Haiden, T., Magnusson, L., Tsonevsky, I., Wetterhall, F., Alfieri, L., Pappenberger, F., De Rosnay, P., Muñoz-Sabater, J., Balsamo, G., Albergel, C., et al.: ECMWF forecast performance during the June 2013 flood in Central Europe, European Centre for Medium-Range Weather Forecasts Reading, MA, 2014.

Haiden, T., Janousek, M., Vitart, F., Ben-Bouallegue, Z., Ferranti, L., and Prates, F.: Evaluation of ECMWF forecasts, including the 2021 upgrade, Tech. rep., 2021a.

1270 Haiden, T., Janousek, M., Vitart, F., Ben Bouallegue, Z., Ferranti, L., Prates, F., and Richardson, D.: Evaluation of ECMWF forecasts, including the 2020 upgrade, European Centre for Medium Range Weather Forecasts, 2021b.

Hamill, T. M., Whitaker, J. S., and Mullen, S. L.: Reforecasts: An important dataset for improving weather predictions, Bulletin of the American Meteorological Society, 87, 33–46, 2006.

Harrigan, S., Zoster, E., Cloke, H., Salamon, P., and Prudhomme, C.: Daily ensemble river discharge reforecasts and real-time forecasts from
1275 the operational Global Flood Awareness System, Hydrology and Earth System Sciences Discussions, pp. 1–22, 2020.

Hemri, S.: Applications of postprocessing for hydrological forecasts, Statistical Postprocessing of Ensemble Forecasts, pp. 219–240, 2018.

Hemri, S., Lisniak, D., and Klein, B.: Multivariate postprocessing techniques for probabilistic hydrological forecasting, Water Resources Research, 51, 7436–7451, 2015a.

Hemri, S., Lisniak, D., and Klein, B.: Multivariate postprocessing techniques for probabilistic hydrological forecasting, Water Resources
1280 Research, 51, 7436–7451, https://doi.org/https://doi.org/10.1002/2014WR016473, 2015b.

Hersbach, H.: Decomposition of the continuous ranked probability score for ensemble prediction systems, Weather and Forecasting, 15, 559–570, 2000.

Hofmann, H., Wickham, H., and Kafadar, K.: Value plots: Boxplots for large data, Journal of Computational and Graphical Statistics, 26, 469–477, 2017.

1285 Jordan, A., Krüger, F., and Lerch, S.: Evaluating Probabilistic Forecasts with scoringRules, Journal of Statistical Software, 90, 1–37, 2019.

Kalman, R. E.: A New Approach to Linear Filtering and Prediction Problems, Journal of Basic Engineering, 82, 35–45, https://doi.org/10.1115/1.3662552, 1960.

Kan, G., He, X., Li, J., Ding, L., Hong, Y., Zhang, H., Liang, K., and Zhang, M.: Computer aided numerical methods for hydrological model calibration: An overview and recent development, Archives of Computational Methods in Engineering, 26, 35–59, 2019.

1290 Kleiber, C. and Kotz, S.: Statistical size distributions in economics and actuarial sciences, vol. 470, John Wiley & Sons, 2003.

Klein, B., Pechlivanidis, I., Arnal, L., Crochemore, L., Meissner, D., and Frielingsdorf, B.: Does the application of multiple hydrological models improve seasonal streamflow forecasting skill?, in: EGU General Assembly Conference Abstracts, p. 20187, 2020.

Kling, H., Fuchs, M., and Paulin, M.: Runoff conditions in the upper Danube basin under an ensemble of climate change scenarios, Journal of Hydrology, 424, 264–277, 2012.

1295 Krzysztofowicz, R.: Bayesian theory of probabilistic forecasting via deterministic hydrologic model, Water Resources Research, 35, 2739–2750, 1999.

Krzysztofowicz, R. and Herr, H. D.: Hydrologic uncertainty processor for probabilistic river stage forecasting: precipitation-dependent model, Journal of hydrology, 249, 46–68, 2001.

Krzysztofowicz, R. and Kelly, K. S.: Hydrologic uncertainty processor for probabilistic river stage forecasting, Water resources research, 36,
1300 3265–3277, 2000.

Krzysztofowicz, R. and Maranzano, C. J.: Hydrologic uncertainty processor for probabilistic stage transition forecasting, Journal of Hydrology, 293, 57–73, 2004.

Lavers, D. A., Harrigan, S., and Prudhomme, C.: Precipitation biases in the ECMWF integrated forecasting system, Journal of Hydrometeorology, 22, 1187–1198, 2021.

1305 Li, W., Duan, Q., Miao, C., Ye, A., Gong, W., and Di, Z.: A review on statistical postprocessing methods for hydrometeorological ensemble forecasting, Wiley Interdisciplinary Reviews: Water, 4, e1246, 2017.

Liu, Y., Weerts, A., Clark, M., Hendricks Franssen, H.-J., Kumar, S., Moradkhani, H., Seo, D.-J., Schwanenberg, D., Smith, P., Van Dijk, A., et al.: Advancing data assimilation in operational hydrologic forecasting: progresses, challenges, and emerging opportunities, Hydrology and Earth System Sciences, 16, 3863–3887, 2012.

1310 Maass, C.: Implementation of IFS Cycle 47r2, https://confluence.ecmwf.int/display/COPSRV/ImplementationofIFScycle47r2, last accessed: 2021-10-07, 2021.

MacDonald, A., Scarrott, C. J., Lee, D., Darlow, B., Reale, M., and Russell, G.: A flexible extreme value mixture model, Computational Statistics & Data Analysis, 55, 2137–2157, 2011.

Mason, D., Garcia Pintado, J., Cloke, H. L., Dance, S., and Munoz-Sabater, J.: Assimilating high resolution remotely sensed soil moisture

1315 into a distributed hydrologic model to improve runoff prediction, ECMWF Technical Memorandum, 2020.

Mason, S. J. and Graham, N. E.: Conditional probabilities, relative operating characteristics, and relative operating levels, Weather and Forecasting, 14, 713–725, 1999.

Mazzetti, C. and Harrigan, S.: What's new in EFAS 4.0? Model improvements, 6-hourly calibration, new evaluation layers reporting points, 2020.

1320 Mazzetti, C., Decremer, D., Barnard, C., Blick, M., Carton de Wiart, C., F, W., and Prudhomme, C.: River discharge and related historical data from the European Flood Awareness System v4.0, https://doi.org/10.24381/cds.e3458969, Accessed: 2021-03-04, 2020.

Mazzetti, C., Decremer, D., and Prudhomme, C.: Challenges of the European Flood Awareness System (EFAS) hydrological calibration, 2021a.

Mazzetti, C., Decremer, D., and Prudhomme, C.: Major upgrade of the European Flood Awareness System, ECMWF Newsletter, available

1325 from: https://www.ecmwf.int/en/newsletter/166/meteorology/major-upgrade-european-flood-awareness-system, 2021b.

McMillan, H., Krueger, T., and Freer, J.: Benchmarking observational uncertainties for hydrology: rainfall, river discharge and water quality, Hydrological Processes, 26, 4078–4111, 2012.

Montani, A., Cesari, D., Marsigli, C., and Paccagnella, T.: Seven years of activity in the field of mesoscale ensemble forecasting by the COSMO-LEPS system: main achievements and open challenges, Tellus A: Dynamic Meteorology and Oceanography, 63, 605–624, 2011.

1330 Pagano, T. C., Shrestha, D. L., Wang, Q., Robertson, D., and Hapuarachchi, P.: Ensemble dressing for hydrological applications, Hydrological Processes, 27, 106–116, 2013.

Pappenberger, F. and Beven, K. J.: Ignorance is bliss: Or seven reasons not to use uncertainty analysis, Water resources research, 42, 2006.

Pappenberger, F., Thielen, J., and Del Medico, M.: The impact of weather forecast improvements on large scale hydrology: analysing a decade of forecasts of the European Flood Alert System, Hydrological Processes, 25, 1091–1113, 2011.

1335 Pappenberger, F., Cloke, H. L., Parker, D. J., Wetterhall, F., Richardson, D. S., and Thielen, J.: The monetary benefit of early flood warnings in Europe, Environmental Science & Policy, 51, 278–291, https://doi.org/https://doi.org/10.1016/j.envsci.2015.04.016, 2015a.

Pappenberger, F., Ramos, M.-H., Cloke, H. L., Wetterhall, F., Alfieri, L., Bogner, K., Mueller, A., and Salamon, P.: How do I know if my forecasts are better? Using benchmarks in hydrological ensemble prediction, Journal of Hydrology, 522, 697–713, 2015b.

R Core Team: R: A Language and Environment for Statistical Computing, R Foundation for Statistical Computing, Vienna, Austria, https:

1340 //www.R-project.org/, 2019.

Reggiani, P., Renner, M., Weerts, A., and Van Gelder, P.: Uncertainty assessment via Bayesian revision of ensemble streamflow predictions in the operational river Rhine forecasting system, Water Resources Research, 45, 2009.

Roundy, J., Duan, Q., and Schaake, J.: Hydrological predictability, scales, and uncertainty issues, Handbook of Hydrometeorological Ensemble Forecasting, pp. 3–31, 2019.

1345   Schaake, J. C., Hamill, T. M., Buizza, R., and Clark, M.: HEPEX: the hydrological ensemble prediction experiment, Bulletin of the American
           Meteorological Society, 88, 1541–1548, 2007.

        Schaeybroeck, B. V. and Vannitsem, S.: Post-processing through linear regression, Nonlinear Processes in Geophysics, 18, 147–160, 2011.

        Seo, D.-J., Herr, H., and Schaake, J.: A statistical post-processor for accounting of hydrologic uncertainty in short-range ensemble streamflow
           prediction, Hydrology and Earth System Sciences Discussions, 3, 1987–2035, 2006.

1350   Shrestha, D. L., Pagano, T., Wang, Q., and Robertson, D.: Application of Ensemble Dressing for Hydrological Applications, in: Geophysical
           Research Abstracts, vol. 13, 2011.

        Silverman, B. W.: Spline smoothing: the equivalent variable kernel method, The annals of Statistics, pp. 898–916, 1984.

        Siqueira, V. A., Weerts, A., Klein, B., Fan, F. M., de Paiva, R. C. D., and Collischonn, W.: Postprocessing continental-scale, medium-range
           ensemble streamflow forecasts in South America using Ensemble Model Output Statistics and Ensemble Copula Coupling, Journal of
1355   Hydrology, 600, 126 520, 2021.

        Skøien, J. O., Bogner, K., Salamon, P., and Wetterhall, F.: On the Implementation of Postprocessing of Runoff Forecast Ensembles, Journal
           of Hydrometeorology, 22, 2731–2749, 2021.

        Smith, P., Pappenberger, F., Wetterhall, F., Thielen del Pozo, J., Krzeminski, B., Salamon, P., Muraro, D., Kalas, M., and Baugh, C.: Chapter
           11 - On the Operational Implementation of the European Flood Awareness System (EFAS), in: Flood Forecasting, edited by Adams, T. E.
1360   and Pagano, T. C., pp. 313–348, Academic Press, Boston, https://doi.org/https://doi.org/10.1016/B978-0-12-801884-2.00011-6, 2016.

        Tabeart, J. M., Dance, S. L., Lawless, A. S., Nichols, N. K., and Waller, J. A.: Improving the condition number of estimated covariance
           matrices, Tellus A: Dynamic Meteorology and Oceanography, 72, 1–19, 2020.

        Takeshi, A.: Advanced econometrics, pp. 125–127, Harvard university press, 1985.

        Thiboult, A., Anctil, F., and Ramos, M.: How does the quantification of uncertainties affect the quality and value of flood early warn-
1365   ing systems?, Journal of Hydrology, 551, 365–373, https://doi.org/https://doi.org/10.1016/j.jhydrol.2017.05.014, investigation of Coastal
           Aquifers, 2017.

        Thielen, J., Bartholmes, J., Ramos, M.-H., and Roo, A. d.: The European flood alert system–Part 1: concept and development, Hydrology
           and Earth System Sciences, 13, 125–140, 2009.

        Todini, E.: A model conditional processor to assess predictive uncertainty in flood forecasting, International Journal of River Basin Manage-
1370   ment, 6, 123–137, 2008.

        Todini, E.: From HUP to MCP: Analogies and extended performances, Journal of hydrology, 477, 33–42, 2013.

        Todini, E., Coccia, G., and Ortiz, E.: On the proper use of ensembles for predictive uncertainty assessment, in: EGU General Assembly
           Conference Abstracts, p. 10365, 2015.

        van Andel, S. J., Weerts, A., Schaake, J., and Bogner, K.: Post-processing hydrological ensemble predictions intercomparison experiment,
1375   Hydrological Processes, 27, 158–161, 2013.

        Van Der Knijff, J., Younis, J., and De Roo, A.: LISFLOOD: a GIS-based distributed model for river basin scale water balance and flood
           simulation, International Journal of Geographical Information Science, 24, 189–212, 2010.

        Venables, W. N. and Ripley, B. D.: Modern Applied Statistics with S, Springer, New York, fourth edn., http://www.stats.ox.ac.uk/pub/
           MASS4, iSBN 0-387-95457-0, 2002.

1380   Verkade, J., Brown, J., Reggiani, P., and Weerts, A.: Post-processing ECMWF precipitation and temperature ensemble reforecasts for opera-
           tional hydrologic forecasting at various spatial scales, Journal of Hydrology, 501, 73–91, 2013.

Verkade, J., Brown, J., Davids, F., Reggiani, P., and Weerts, A.: Estimating predictive hydrological uncertainty by dressing deterministic and ensemble forecasts; a comparison, with application to Meuse and Rhine, Journal of Hydrology, 555, 257–277, 2017.

Weerts, A., Winsemius, H., and Verkade, J.: Estimation of predictive hydrological uncertainty using quantile regression: examples from the National Flood Forecasting System (England and Wales), Hydrology and Earth System Sciences, 15, 255–265, 2011.

Węglarczyk, S.: Kernel density estimation and its application, in: ITM Web of Conferences, vol. 23, EDP Sciences, 2018.

Wu, W., Emerton, R., Duan, Q., Wood, A. W., Wetterhall, F., and Robertson, D. E.: Ensemble flood forecasting: Current status and future opportunities, Wiley Interdisciplinary Reviews: Water, 7, e1432, 2020.

Ye, A., Duan, Q., Yuan, X., Wood, E. F., and Schaake, J.: Hydrologic post-processing of MOPEX streamflow simulations, Journal of hydrology, 508, 147–156, 2014.

Zamo, M. and Naveau, P.: Estimation of the continuous ranked probability score with limited information and applications to ensemble weather forecasts, Mathematical Geosciences, 50, 209–234, 2018.

Zängl, G., Reinert, D., Rípodas, P., and Baldauf, M.: The ICON (ICOsahedral Non-hydrostatic) modelling framework of DWD and MPI-M: Description of the non-hydrostatic dynamical core, Quarterly Journal of the Royal Meteorological Society, 141, 563–579, 2015.

Zhao, L., Duan, Q., Schaake, J., Ye, A., and Xia, J.: A hydrologic post-processor for ensemble streamflow predictions, Advances in Geosciences, 29, 51–59, 2011.

Zhong, Y., Guo, S., Xiong, F., Liu, D., Ba, H., and Wu, X.: Probabilistic forecasting based on ensemble forecasts and EMOS method for TGR inflow, Frontiers of Earth Science, 14, 188–200, 2020.

Škute, A., Gruberts, D., Soms, J., and Paidere, J.: Ecological and hydrological functions of the biggest natural floodplain in Latvia, Ecohydrology & Hydrobiology, 8, 291–306, https://doi.org/https://doi.org/10.2478/v10104-009-0023-y, 2008.